PCH-2^{TRIP13} regulates spindle checkpoint strength

Lénaïg Défachelles, Anna E. Russo, Christian R. Nelson and Needhi Bhalla*

Department of Molecular, Cell and Developmental Biology, University of California, Santa Cruz,

Santa Cruz, CA 95064

*corresponding author: nbhalla@ucsc.edu

Department of Molecular, Cell and Developmental Biology

225 Sinsheimer Labs

University of California, Santa Cruz

Santa Cruz, CA 95064

phone: (831) 459-1319

fax: (831) 459-3139

Key words: *C. elegans*, mitosis, embryo, spindle assembly checkpoint, Mad2, aneuploidy, germline

ABSTRACT

Spindle checkpoint strength is dictated by three criteria: the number of unattached kinetochores, cell volume and cell fate. We show that the conserved AAA-ATPase, PCH-2/TRIP13, which remodels the checkpoint effector Mad2 from an active conformation to an inactive one, controls checkpoint strength in *C. elegans*. When we genetically manipulate embryos to decrease cell volume, PCH-2 is no longer required for the spindle checkpoint or recruitment of Mad2 at unattached kinetochores in embryos with monopolar spindles. This role in checkpoint strength is not limited to large cells: the stronger checkpoint in germline precursor cells also depends on PCH-2. PCH-2 is enriched in germline precursor cells and this enrichment relies on a conserved factor that induces asymmetry in the early embryo. Finally, the stronger checkpoint in germline precursor cells is regulated by CMT-1, the *C. elegans* ortholog of $p31^{comet}$, which is required for both PCH-2's localization to unattached kinetochores and its enrichment in germline precursor cells. Thus, PCH-2, likely through its ability to regulate the availability of inactive Mad2 at and near unattached kinetochores, governs checkpoint strength.

INTRODUCTION

To prevent the missegregation of chromosomes and the production of daughter cells with an incorrect number of chromosomes, the spindle checkpoint (also called the spindle assembly checkpoint) monitors whether chromosomes are attached to the spindle via kinetochores. If kinetochores fail to attach properly, this checkpoint delays the cell cycle to promote error correction and prevent aneuploidy. Despite its critical role, the duration of the cell cycle delay, defined as the strength of the spindle checkpoint, can be highly variable. This variability can be controlled by the number of unattached kinetochores (Collin, Nashchekina et al., 2013), cell volume (Galli & Morgan, 2016, Kyogoku & Kitajima, 2017), and cell fate (Galli & Morgan, 2016, Gerhold, Poupart et al., 2018).

The spindle checkpoint response initiates with the recruitment of Mad1 and Mad2 at unattached kinetochores (Chen, Shevchenko et al., 1998, Chen, Waters et al., 1996, Li & Benezra, 1996, Sironi, Melixetian et al., 2001), which catalyzes the production of a Mitotic Checkpoint Complex (MCC). The MCC enforces a checkpoint arrest by inhibiting the Anaphase Promoting Complex/Cyclosome (APC/C) and preventing cell cycle progression (Sudakin, Chan et al., 2001). Formation of the MCC is driven by conformational changes in Mad2, which can exist in an open conformation (O-Mad2) or a closed conformation (C-Mad2) (Luo, Tang et al., 2002, Luo, Tang et al., 2004, Sironi, Mapelli et al., 2002). Mad2 is in the closed conformation in the Mad1/Mad2 tetramer recruited to unattached kinetochores. C-Mad2 in the tetramer acts as a template to convert additional soluble O-Mad2 to C-Mad2, which can be assembled into the MCC (De Antoni, Pearson et al., 2005, Fava, Kaulich et al., 2011, Simonetta, Manzoni et al., 2009, Sironi et al., 2001). Thus, unattached kinetochores act as a platform for MCC

69 assembly. The MCC effectively tunes the spindle checkpoint response: the length of the
70 cell cycle delay imposed by the checkpoint is governed by the ratio of the soluble MCC
71 checkpoint signal to cytoplasmic volume (Collin et al., 2013, Dick & Gerlich, 2013, Galli
72 & Morgan, 2016, Kyogoku & Kitajima, 2017).
73
74 PCH-2/TRIP13 is a hexameric AAA+ ATPase that remodels HORMA domain-containing
75 proteins, a group that includes Mad2 (Aravind & Koonin, 1998, Rosenberg & Corbett,
76 2015, Vader, 2015). Originally described as a spindle checkpoint silencing protein,
77 experiments showed that TRIP13 works with the adaptor protein p31^{comet} to extract C-
78 Mad2 from the MCC and promote its disassembly, permitting the activation of the APC/C
79 (Alfieri, Chang et al., 2018, Brulotte, Jeong et al., 2017, Eytan, Wang et al., 2014,
80 Miniowitz-Shemtov, Eytan et al., 2015, Wang, Sturt-Gillespie et al., 2014, Ye, Rosenberg
81 et al., 2015). We and others have shown that PCH-2/TRIP13 is essential for spindle
82 checkpoint activation in *C. elegans* and mammalian cells (Ma & Poon, 2016, Ma & Poon,
83 2018, Nelson, Hwang et al., 2015, Yost, de Wolf et al., 2017). PCH-2 is present at
84 unattached kinetochores (Nelson et al., 2015, Tipton, Wang et al., 2012, Wang et al.,
85 2014) and is required to robustly localize Mad2, but not Mad1, to unattached
86 kinetochores (Nelson et al., 2015, Yost et al., 2017). Biochemical and structural studies
87 have shown that PCH-2 converts C-Mad2 to O-Mad2 (Alfieri et al., 2018, Brulotte et al.,
88 2017, Ye et al., 2015). Altogether, these data suggest a model in which PCH-2 converts
89 a population of C-Mad2 that is not competent for checkpoint signaling into O-Mad2, so
90 that Mad1/Mad2 recruited to unattached kinetochores can template C-Mad2 for
91 assembly into the MCC.
92
93 This model has major implications for our understanding of the spindle checkpoint. First,
94 it indicates that the spindle checkpoint does not simply depend on the presence of C-

95 Mad2. Rather, only C-Mad2 that has been assembled into the MCC at unattached
96 kinetochores is competent for checkpoint signaling (Ma & Poon, 2016). Second, it
97 suggests that there is a significant population of C-Mad2 in cells that must be liberated
98 for a functional checkpoint. In *C. elegans*, some of this C-Mad2 appears to be
99 complexed with and stabilized by the Mad2 mimic p31^{comet} (CMT-1 in *C. elegans*)
100 (Nelson et al., 2015, Yang, Li et al., 2007); loss of CMT-1 partially suppresses the
101 spindle checkpoint defect in *pch-2* mutants, likely by liberating enough O-Mad2 to make
102 PCH-2 partially dispensable (Nelson et al., 2015). In cells that have a significant
103 population of available O-Mad2, such as HeLa cells (Luo et al., 2004), TRIP13 function
104 becomes essential for checkpoint activity only when this population of O-Mad2 is limiting
105 (Ma & Poon, 2018).
106
107 Here, we show that PCH-2 controls spindle checkpoint strength in *C. elegans*. Despite
108 being essential for the spindle checkpoint in the large somatic, or AB, cell of the two-cell
109 embryo (Nelson et al., 2015), PCH-2 becomes dispensable for the spindle checkpoint
110 and Mad2 recruitment at unattached kinetochores as AB cells are genetically
111 manipulated to become smaller, suggesting that PCH-2's ability to concentrate O-Mad2
112 near unattached kinetochores is essential for checkpoint activation in large cells. Indeed,
113 robust spindle checkpoint strength relies on Mad2 dosage. The requirement for PCH-2 in
114 promoting spindle checkpoint strength is also observed in germline precursor, or P_1,
115 cells, which have a stronger checkpoint than their somatic counterparts. PCH-2 is
116 enriched in P_1 cells and this enrichment depends on a conserved regulator of embryonic
117 polarity, PAR-1. Further, the stronger checkpoint in P_1 cells also relies on the *C. elegans*
118 ortholog of p31^{comet}, CMT-1, suggesting that CMT-1's role in localizing PCH-2 to
119 unattached kinetochores and its ability to enrich PCH-2 in P_1 cells, contributes to a
120 stronger checkpoint. We propose that PCH-2, and its mammalian ortholog TRIP13,

121 ensure a robust spindle checkpoint response and proper chromosome segregation by
122 regulating the availability of O-Mad2 at and near unattached kinetochores. This role may
123 be specifically relevant in scenarios where maintaining genomic stability is particularly
124 challenging, such as in oocytes and early embryos enlarged for developmental
125 competence and germline cells that maintain immortality.
126
127 **RESULTS**
128
129 **PCH-2 becomes dispensable for the spindle checkpoint response in somatic cells**
130 **experimentally reduced in size**
131 In the large somatic, or AB, cell of the *C. elegans* two-cell embryo, PCH-2 is essential for
132 spindle checkpoint activation (Nelson et al., 2015). To further assess the requirements
133 for PCH-2 function, we manipulated the cell volume of AB cells experimentally by
134 performing RNA interference (RNAi) against *ani-2*. *ani-2* encodes a germline specific
135 anillin whose depletion generates oocytes and, after fertilization, embryos, of varying
136 size (Maddox, Habermann et al., 2005) (Figure 1A). We monitored the length of mitosis
137 in these embryos, using the time between nuclear envelope breakdown (NEBD) to the
138 onset of cortical contractility (OCC) as markers for the entry into and exit from mitosis,
139 respectively (Essex, Dammermann et al., 2009). We then correlated the length of mitosis
140 to cytoplasmic volume. RNAi of *ani-2* did not affect cell cycle progression in control, *pch-*
141 *2*, or *mad-1* mutants (Figure S1A), indicating that reducing cytoplasmic volume did not
142 affect mitotic timing in these embryos. (In *C. elegans*, the genes that encode Mad1 and
143 Mad2 are *mdf-1* and *mdf-2*, respectively. To avoid confusion, we will use *mad-1* and
144 *mad-2*).
145

146 We performed double depletion of *ani-2* and *zyg-1* to induce the spindle checkpoint
147 response in control embryos, *pch-2*, and *mad-1* mutants. ZYG-1 is essential for
148 centrosome duplication and after the first embryonic division, its depletion generates
149 monopolar spindles (O'Connell, Caron et al., 2001) and unattached kinetochores (Essex
150 et al., 2009) (Figure 1B). Consistent with previous reports, as cells decreased in cell
151 volume the length of the cell cycle delay, an indicator of spindle checkpoint strength,
152 increased in control embryos (Galli & Morgan, 2016, Gerhold et al., 2018) (Figure 1C,
153 Videos 1 and 2). Surprisingly, as *pch-2* mutant embryos decreased in size, the spindle
154 checkpoint response more closely resembled that of control embryos than *mad-1* mutant
155 embryos (Figure 1C, Videos 3 and 4). There was no significant difference between the
156 slopes of the regression analysis of control and *pch-2* mutant data (p value = 0.1407),
157 while the slopes between the regression analysis of *pch-2* and *mad-1* mutant data were
158 significantly different (p value = 0.0007). We partitioned our data to show that *pch-2*
159 mutant embryos fell into three clear categories: 1) wild-type sized embryos (more than 5
160 x 10^3 μm^3) in which PCH-2 was essential for the spindle checkpoint; 2) medium sized
161 embryos (between 3.5 x 10^3 μm^3 and 5 x 10^3 μm^3), which exhibited an intermediate level
162 of checkpoint function; and 3) small embryos (less than 3.5 x 10^3 μm^3), in which PCH-2
163 was completely dispensable for the spindle checkpoint response (Figure 1D).
164
165 We verified that the mitotic delay observed in *pch-2* embryos was a legitimate spindle
166 checkpoint response by monitoring mitotic timing after performing double depletion of
167 *ani-2* and *zyg-1* in *san-1* and *pch-2;san-1* mutant embryos. SAN-1 is the *C. elegans*
168 ortholog of the essential spindle checkpoint factor, Mad3 (Nystul, Goldmark et al., 2003)
169 (Figure S1B). There was no significant difference between the slopes of the regression
170 analysis of *san-1* and *pch-2;san-1* data (p value = 0.8813). These data allow us to draw
171 two important conclusions: 1) Since we observe a robust spindle checkpoint activation in

172 *pch-2* mutant embryos as they decrease in size and mitotic timing is similar to what we
173 observe in control embryos, PCH-2 does not appear to affect spindle checkpoint
174 silencing in *C. elegans*; and 2) the requirement for PCH-2 during spindle checkpoint
175 activation is proportional to cell volume in somatic cells of two-cell *C. elegans* embryos
176 with monopolar spindles.
177
178
179 Recent experiments have shown that acute depletion of PCH-2's mammalian ortholog,
180 TRIP13, has no effect on spindle checkpoint function in HeLa cells until O-Mad2 is
181 limiting (Ma & Poon, 2018). Since MAD-2 is localized to the nucleus and nuclear
182 envelope in *C. elegans* oocytes (Bohr, Nelson et al., 2015, Lawrence, Chau et al., 2015)
183 (Figure 2A) and *ani-2*^{RNAi} treatment does not affect nuclear size (Figure S2), we
184 reasoned that as cells are genetically manipulated to decrease in cell volume, the
185 absolute amount of MAD-2 protein is likely to remain constant but its concentration
186 increases. This increase in concentration may improve the likelihood that O-Mad2 is at
187 or near unattached kinetochores in embryos treated with *zyg-1* RNAi (Figure 2B),
188 obviating the requirement for PCH-2 in small embryos.
189
190 To test this model, we initially attempted to directly visualize O-Mad2 in *C. elegans*
191 embryos. Unfortunately, we were unable to perform this experiment with a commercial
192 antibody (data not shown). Further, we could not directly probe total Mad2 concentration
193 as cells decrease in volume upon treatment with *ani-2* RNAi because GFP::MAD-2 does
194 not localize to the nucleus and instead localizes in the cytoplasm until NEBD (Essex et
195 al., 2009, Nelson et al., 2015), making it an inaccurate reporter for this assay. Instead,
196 we tested whether reducing Mad2 dosage affected checkpoint strength. We
197 hypothesized that if Mad2 concentration influences checkpoint strength, reducing it by

198 half should attenuate checkpoint strength in comparison to control animals. We
199 performed double depletion of *ani-2* and *zyg-1* in *mad-2* heterozygotes, which express
200 half of the Mad2 of control animals (data not shown). Indeed, *mad-2* heterozygotes
201 exhibited stronger spindle checkpoint strength as AB cells became smaller but not as
202 robustly as control embryos (Figure 2C, Videos 5-8). The slopes of the linear
203 regressions for both control and *mad-2* heterozygotes were significantly non-zero (p
204 value = 0.0002 for control and p = .0395 for *mad-2/+*), unlike similar experiments with
205 *mad-1* homozygotes (p value = 0.4197) (Figure 1B). We could not test whether a
206 decrease in Mad2 protein levels restored the reliance on PCH-2 in small embryos since
207 *pch-2;mad-2/+* double mutants exhibited a substantial decrease in the production of
208 embryos (brood size), preventing us from performing these experiments (data not
209 shown). Further, *pch-2;mad-2* double mutants could not be recovered from *pch-2;mad-*
210 *2/+* mothers (data not shown), a genetic interaction that demonstrates the close
211 functional relationship between these two genes and is not observed when we generate
212 *pch-2;mad-1* double mutants (Bohr et al., 2015) or *pch-2;san-1* double mutants (Figure
213 S1B).
214
215 **PCH-2 becomes dispensable for MAD-2 recruitment at unattached kinetochores in**
216 **somatic cells as they decrease in size**
217
218 Having established that Mad2 dosage affects spindle checkpoint strength (Figure 2C),
219 we reasoned that if our model was correct, we should see increased recruitment of
220 GFP::MAD-2 at unattached kinetochores in small *pch-2* mutant embryos. We quantified
221 GFP::MAD-2 recruitment at unattached kinetochores in pseudo-metaphase in small
222 control and *pch-2* mutant embryos (less than 3.5 x 10^3 μm^3) and compared it to the
223 recruitment observed in wild-type sized embryos. Consistent with our previous results,

224 GFP::MAD-2 was recruited to 20% of control levels in *pch-2* mutant embryos that were
225 wild-type in size (Nelson et al., 2015) (Figures 2D and E). In small embryos, GFP::MAD-
226 2 was recruited to unattached kinetochores in control embryos as expected (Figure 2D).
227 In small *pch-2* mutant embryos, GFP::MAD-2 signal can be detected at unattached
228 kinetochores (Figure 2D) and, when quantified, GFP::MAD-2 was partially restored to
229 58% of control levels (Figure 2E).
230
231 One explanation for why GFP::MAD-2 recruitment is not completely restored in small
232 *pch-2;ani-2*^{RNAi}*;zyg-1*^{RNAi} mutant embryos may be that these smaller embryos require
233 less MAD-2 recruitment to support a mitotic delay than control small embryos
234 (Defachelles, Hainline et al., 2015). Consistent with this idea, when we plotted
235 GFP::MAD-2 fluorescence against cell volume, we observed that the regression analysis
236 of GFP::MAD-2 fluorescence at unattached kinetochores in *pch-2;ani-2*^{RNAi}*;zyg-1*^{RNAi}
237 embryos exhibited a negative slope, showing improved GFP::MAD-2 recruitment to
238 unattached kinetochores as cells got smaller, but that was nonetheless lower in
239 fluorescence intensity than *ani-2*^{RNAi}*;zyg-1*^{RNAi} control embryos (Figure S3A).
240 Surprisingly, the regression analysis for control embryos had a positive slope,
241 suggesting that less GFP::MAD-2 is required at unattached kinetochores for spindle
242 checkpoint function even in small control embryos (Figure S3A). This was despite similar
243 levels of soluble GFP::MAD2 in both genetic backgrounds (Figure S3B). Nevertheless,
244 our experiments demonstrate that PCH-2 is also dispensable for Mad2 recruitment at
245 unattached kinetochores in small embryos with monopolar spindles, potentially because
246 decreasing cell volume concentrates Mad2, specifically O-Mad2 around mitotic
247 chromosomes.
248

249 **PCH-2 is essential for the spindle checkpoint in *ani-2^{RNAi}* small embryos treated**
250 **with nocodazole**
251
252 Next, we evaluated whether PCH-2 became dispensable for the spindle checkpoint as
253 cells decreased in size when the spindle checkpoint was activated by spindle
254 depolymerizing drugs. We permeabilized embryos by performing *perm-1* RNAi
255 (Carvalho, Olson et al., 2011) and activated the spindle checkpoint by treating these
256 *perm-1^{RNAi}* embryos with nocodazole, a drug that depolymerizes microtubules. Since we
257 could not reliably visualize OCC in these dividing embryos, we measured mitotic timing
258 from nuclear envelope break down (NEBD) to decondensation of chromosomes
259 (DECON) in the AB cells of two cell embryos. To our surprise, when *pch-2;ani-*
260 *2^{RNAi};perm-1^{RNAi}* embryos were treated with the microtubule depolymerizing drug,
261 nocodazole, PCH-2 remained essential for the spindle checkpoint, similar to *san-1;ani-*
262 *2^{RNAi};perm-1^{RNAi}* mutants and unlike *ani-2^{RNAi};perm-1^{RNAi}* embryos (Figure 3A, Videos 9-
263 11).
264
265 We wondered whether this greater reliance on PCH-2 in embryos treated with
266 nocodazole was because PCH-2's localization was affected by microtubule
267 depolymerization. In the AB cell, PCH-2 protein becomes enriched in the area around
268 the chromosomes in prometaphase and is recruited to unattached kinetochores if the
269 spindle checkpoint is active (Nelson et al., 2015). Once NEBD occurred, we could easily
270 see PCH-2::GFP coalesce around mitotic chromosomes in a diffuse cloud in control
271 (bipolar spindle), *zyg-1^{RNAi}* (mono-polar spindle) and nocodazole treated (no spindle)
272 embryos (Figure 3B), indicating that PCH-2::GFP localization around chromosomes was
273 not dependent on the spindle. Unfortunately, PCH-2::GFP was difficult to visualize on
274 unattached kinetochores of holocentric chromosomes in nocodazole-treated embryos

275 given the lack of a clear metaphase or pseudo-metaphase plate (data not shown).
276 Instead, we quantified PCH-2::GFP around mitotic chromosomes in control, *zyg-1*^{RNAi}
277 and nocodazole treated embryos after NEBD (Figure 3C). PCH-2::GFP fluorescence
278 around chromosomes was similar in both *zyg-1*^{RNAi} and nocodazole-treated embryos and
279 both were higher than control embryos (Figure 3C). However, we noticed that the area
280 occupied by PCH-2::GFP in nocodazole treated embryos was not significantly different
281 than that of control embryos but significantly larger than that of *zyg-1*^{RNAi} embryos (yellow
282 dashed circle in Figure 3B and quantified in Figure 3D). When we factored this larger
283 area of PCH-2::GFP fluorescence into our analysis, we observed an increase in the
284 integrated density of PCH-2::GFP around mitotic chromosomes in nocodazole treated
285 embryos compared to either *zyg-1*^{RNAi} or control embryos (Figure 3E). Therefore, this
286 increased amount of PCH-2::GFP around mitotic chromosomes in embryos treated with
287 nocodazole may result in a stronger reliance on PCH-2, even in small cells. Alternatively,
288 the dependence on PCH-2 in nocodazole-treated small cells for the spindle checkpoint
289 may reflect a synthetic spindle checkpoint defect: the absence of both PCH-2 and some
290 other factor whose localization or function depends on the spindle prevents full spindle
291 checkpoint activation. This second interpretation is supported by the observation that
292 checkpoint strength increases similarly in nocodazole treated developing embryos to
293 embryos in which *zyg-1* is inactivated (Gerhold et al., 2018), despite having more
294 unattached kinetochores, raising the possibility that a factor required for checkpoint
295 strength may depend on microtubules for function.
296
297 **PCH-2 is required for the spindle checkpoint response during embryogenesis**
298 During embryogenesis, cell volume decreases and spindle checkpoint strength
299 increases (Galli & Morgan, 2016, Gerhold et al., 2018). Given our observation, that PCH-

300 2 becomes dispensable as cell volume decreases in the AB cell of two-cell embryos, we
301 assessed whether this also happens during normal embryogenesis.
302
303 We first performed this experiment in *perm-1*^{RNAi} embryos treated with nocodazole. Cells
304 of the AB lineage in control embryos exhibited a longer mitotic delay in 16-cell than in 4-
305 cell embryos (Figure 4A), verifying that the spindle checkpoint increases in strength as
306 cells decrease in volume during embryogenesis (Galli & Morgan, 2016, Gerhold et al.,
307 2018). As a control, we performed the same experiment in *san-1* mutants and did not
308 detect a mitotic delay when these embryos were treated with nocodazole (Figure 4A).
309 Consistent with the results that PCH-2 is required in small AB cells treated with
310 nocodazole (Figure 3A), *pch-2* mutant embryos treated with nocodazole resembled *san-*
311 *1* mutants (Figure 4A). Thus, as cells of the AB lineage naturally decrease in cell size
312 during embryogenesis, PCH-2 is essential for the spindle checkpoint when microtubules
313 are absent.
314
315 Given the different requirements for PCH-2 in spindle checkpoint activation in *ani-2*^{RNAi}
316 embryos (Figures 1C and 3A), we also analyzed the requirement for PCH-2 in embryos
317 with monopolar spindles. To perform this experiment, we used a fast acting temperature
318 sensitive allele of *zyg-1* (*zyg-1*^{ts}) (O'Rourke, Carter et al., 2011) to activate the spindle
319 checkpoint in developing embryos with a variable number of cells. We shifted embryos
320 at different stages of development, verified the appearance of monopolar spindles and
321 measured mitotic timing from NEBD to DECON. In control *zyg-1*^{ts} mutant embryos, we
322 observed a delay in mitotic timing in cells from the AB lineage and this delay only
323 became marginally longer as embryos had more cells (Figure 4B), similar to previous
324 reports (Gerhold et al., 2018). In stark contrast to our *ani-2*^{RNAi} experiments, the mitotic
325 timing observed in *pch-2;zyg-1*^{ts} mutant embryos was reduced in comparison to *zyg-1*^{ts}

326 embryos. Thus, similar to our results with embryos treated with nocodazole, PCH-2 is
327 required for the spindle checkpoint as cells of the AB lineage naturally decrease in cell
328 size during embryogenesis and when the checkpoint is activated by the presence of
329 monopolar spindles. However, additional considerations may make direct comparisons
330 between our *ani-2*^{RNAi}*;zyg-1* ^{RNAi} experiments and *zyg-1*^{ts} dividing embryos difficult (see
331 Discussion).
332
333 **PCH-2 is responsible for the stronger spindle checkpoint in the germline lineage**
334 Cell fate is another important determinant of spindle checkpoint strength. In *C. elegans*
335 embryos, the spindle checkpoint is stronger in germline precursor cells than similarly
336 sized somatic counterparts (Galli & Morgan, 2016, Gerhold et al., 2018).
337 Therefore, we tested whether PCH-2 contributed to the stronger spindle checkpoint in
338 the germline lineage, specifically in P_1 cells of two-cell embryos (Figures 5 and S4).
339 Consistent with other reports (Galli & Morgan, 2016, Gerhold et al., 2018), when we
340 performed double depletion of *ani-2* and *zyg-1* in control embryos and monitored mitotic
341 timing, we observed P_1 cells with similar volumes as AB cells exhibiting a longer cell
342 cycle delay (Figures 5A and S4, Videos 12 and 13). Further, the regression analysis that
343 best fit control P_1 data is significantly different and steeper than that of control AB cells (p
344 value < 0.0001), indicating that variables in addition to cell volume contribute to the
345 spindle checkpoint strength in germline precursor cells. When we knocked down both
346 *ani-2* and *zyg-1* in *pch-2* mutant embryos, we no longer observed a significant difference
347 (p value = 0.9096) between the slopes of the regression analysis of P_1 and AB cells
348 (Figures 5B and S4, Videos 14 and 15), indicating that PCH-2 is responsible for the
349 stronger checkpoint in P_1 cells.
350

351 We observed that cell cycle timing was faster in *pch-2* mutant P_1 cells than similarly
352 sized *pch-2* mutant AB cells after treatment with *ani-2* and *zyg-1* RNAi (Figures 5B and
353 S4). We wondered if embryonic germline precursor cells might rely on some spindle
354 checkpoint proteins for normal mitotic timing, analogous to mitotically dividing stem cells
355 in the *C. elegans* germline (Gerhold, Ryan et al., 2015) and similar to mammalian
356 cultured cells (Ma & Poon, 2016, Meraldi, Draviam et al., 2004, Rodriguez-Bravo,
357 Maciejowski et al., 2014). To address this, we measured normal mitotic timing in AB and
358 P_1 cells of both control and *pch-2* mutant embryos. We found that while normal mitotic
359 timing is unaffected by mutation of *pch-2* in AB cells, *pch-2* mutant P_1 cells go through
360 mitosis significantly faster than control P_1 cells (Figure 5C), thus providing an
361 explanation for the faster cell cycle timing in *pch-2* mutant P_1 cells with the same cell
362 volume as *pch-2* mutant AB cells after treatment with *ani-2* and *zyg-1* RNAi. We saw a
363 decrease in the cell cycle timing of P_1 cells in *mad-1* mutants but this was not statistically
364 different than control P_1 cells (Figure 5C).
365

366 **PCH-2's enrichment in P_1 cells is dependent on PAR-1**

367 Cell fate is driven by the asymmetric distribution of various determinants between
368 somatic and germline lineages during early divisions of the *C. elegans* embryo (Rose &
369 Gonczy, 2014). Since we found that PCH-2 promoted the spindle checkpoint strength in
370 both AB and P_1 cells, but even more dramatically in P_1 cells, we asked if PCH-2 was
371 regulated differently between these cells. First, we tested whether PCH-2::GFP could
372 also support the stronger checkpoint in P_1 cells. We treated embryos expressing PCH-
373 2::GFP with *zyg-1* RNAi and evaluated mitotic timing in both AB and P_1 cells, in the
374 presence or absence of monopolar spindles, using chromosome decondensation as a

375 marker for mitotic exit. P_1 cells expressing PCH-2::GFP had full checkpoint function,
376 exhibiting a mitotic delay longer than AB cells also expressing PCH-2::GFP (Figure 6A).
377
378 Previous transcriptome analysis of PCH-2 did not reveal asymmetric enrichment of PCH-
379 2 mRNA between AB and P_1 cells (Tintori, Osborne Nishimura et al., 2016). We tested
380 whether PCH-2::GFP exhibited differences in protein levels between AB and P_1 cells.
381 First, we assessed whether PCH-2::GFP was more enriched in pseudo-metaphase at
382 unattached kinetochores in P_1 than AB cells. We quantified PCH-2::GFP fluorescence at
383 unattached kinetochores in both AB and P_1 cells of embryos treated with *zyg-1* RNAi but
384 did not detect any difference between the two cell types (Figures S5A and B). Similarly,
385 we did not detect any difference in GFP::MAD-2 recruitment at unattached kinetochores
386 between AB and P_1 cells in *zyg-1*^{RNAi} embryos (Figures S5C and D).
387
388 Since neither PCH-2::GFP or GFP::MAD-2 recruitment to unattached kinetochores were
389 different between AB and P_1 cells (Figure S5) and given the existence of a “cloud” of
390 checkpoint factors, including MAD-2 and PCH-2, around chromosomes, even during
391 normal cell cycles (Essex et al., 2009, Nelson et al., 2015), we quantified PCH-2::GFP
392 fluorescence around mitotic chromosomes in AB and P_1 cells during unperturbed cell
393 cycles. Similar to AB cells (Nelson et al., 2015), we observed PCH-2::GFP enriched in
394 the area around the chromosomes in prometaphase in P_1 cells (Figure 6B). When we
395 quantified the fluorescence of PCH-2::GFP in this area surrounding chromosomes after
396 NEBD in both AB and P_1 cells, we detected a statistically significant enrichment of PCH-
397 2::GFP in P_1 cells (Figure 6C). To evaluate whether this enrichment was the indirect
398 consequence of the smaller volume of P_1 cells, we also quantified PCH-2::GFP
399 fluorescence in *gpr-1/2*^{RNAi} embryos. This double knockdown equalizes the size of AB
400 and P_1 cells without affecting their cell fate (Colombo, Grill et al., 2003, Gotta, Dong et

401 al., 2003, Srinivasan, Fisk et al., 2003). *gpr-1/2*^{RNAi} embryos showed a similar
402 enrichment of PCH-2::GFP in P_1 cells as control embryos (Figure S7).
403
404 To better understand the relationship between PCH-2 enrichment in P_1 cells and cell
405 fate, we abrogated the asymmetry of the two-cell embryo by performing RNAi against
406 the essential polarity factor, PAR-1 (Guo & Kemphues, 1995). In *par-1*^{RNAi} mutant
407 embryos, both AB and P_1 cells exhibit the same checkpoint strength as control P_1 cells
408 (Gerhold et al., 2018), indicating that the stronger spindle checkpoint response in the P_1
409 cells depends on this asymmetric division. Despite the loss of cell fate in *par-1*^{RNAi}
410 embryos, we will refer to the anterior blastomere as AB and the posterior as P_1. We
411 quantified PCH-2::GFP fluorescence in the area around chromosomes in AB and P_1
412 cells after *par-1* RNAi and observed that the fluorescence of PCH-2::GFP, despite being
413 slightly lower in P_1 cells, was not significantly different between AB and P_1 cells, unlike
414 what we observed in embryos exposed to control RNAi (Figures 6D and E). Further,
415 similar to the effect on spindle checkpoint strength (Gerhold et al., 2018), we found that
416 the concentration of PCH-2::GFP in *par-1*^{RNAi} AB cells was greater than that of control
417 AB cells (data not shown) and more closely resembled PCH-2::GFP concentration in P_1
418 cells treated with control RNAi (p value = 0.348). Therefore, PCH-2::GFP's enrichment
419 around mitotic chromosomes in P_1 cells depends on a conserved factor that induces
420 embryonic asymmetry and germline cell fate, PAR-1.
421
422 **The stronger checkpoint in P_1 cells depends on CMT-1**
423 In vitro, the *C. elegans* ortholog of p31^{comet}, CMT-1, is required for PCH-2 to bind and
424 remodel Mad2 (Ye et al., 2015). In addition to this role, CMT-1 is also required to localize
425 PCH-2 to unattached kinetochores during the spindle checkpoint response, stabilize
426 Mad2 protein levels and generate a robust spindle checkpoint response in AB cells

427 (Nelson et al., 2015). Overexpressing Mad2 does not suppress the partial defect in
428 spindle checkpoint activation in *cmt-1* mutants (Nelson et al., 2015), suggesting that
429 PCH-2's localization to unattached kinetochores promotes a strong spindle checkpoint
430 response in large AB cells. Therefore, we reasoned that CMT-1 might also be required
431 for the stronger checkpoint in P_1 cells.
432
433 To test this possibility, we first performed double knockdown of *ani-2* and *zyg-1* in *cmt-1*
434 mutants and monitored the length of the spindle checkpoint response as AB and P_1 cells
435 became smaller (Figure 7A, Videos 16-19). Similar to *pch-2;ani-2*^{RNAi}*;zyg-1*^{RNAi} mutants
436 (Figure 5B), the stronger spindle checkpoint response in P_1 cells was lost in *cmt-1;ani-*
437 *2*^{RNAi}*;zyg-1*^{RNAi} mutants and we did not observe any statistical difference between the
438 between the slopes of the regression analysis of P_1 and AB cells (p value = 0.9403). We
439 also observed that cell cycle timing was faster in *cmt-1* P_1 cells that were similar in
440 volume to *cmt-1* AB cells. Thus, CMT-1 is also essential to promote spindle checkpoint
441 strength in germline precursor cells.
442
443 We also performed *zyg-1* RNAi on control and *cmt-1* mutant embryos and monitored
444 mitotic timing in both AB and P_1 cells. AB and P_1 cells of control and *cmt-1* mutant
445 embryos treated with control RNAi had similar mitotic timing. Unlike similar experiments
446 in *pch-2* mutants (Figure 5C), we did not detect a statistically significant difference
447 between cell cycle time in P_1 cells between wildtype and *cmt-1* mutants embryos (Figure
448 7B), suggesting that *ani-2*^{RNAi}*;zyg-1*^{RNAi} embryos might be more sensitive to subtle
449 perturbations in cell cycle timing. In *zyg-1*^{RNAi} embryos, P_1 cells exhibited a stronger
450 checkpoint response than AB cells (Figure 7B). By contrast, both AB and P_1 cells in *cmt-*
451 *1*;*zyg-1*^{RNAi} mutant embryos exhibited similar spindle checkpoint delays (Figure 7B).

452 Despite having spindle checkpoint responses that were less robust than that of control
453 *zyg-1*^{RNAi} embryos, AB and P_1 cells in *cmt-1* mutant embryos treated with *zyg-1* RNAi
454 spent significantly longer in mitosis than *cmt-1* mutant embryos treated with control RNAi
455 (Figure 7B), indicating that they activated a weaker spindle checkpoint response, similar
456 to our published results (Nelson et al., 2015). More importantly, *cmt-1*;*zyg-1*^{RNAi} mutant
457 embryos failed to generate a stronger checkpoint in P_1 cells, consistent with *cmt-1;ani-*
458 *2*^{RNAi}*;zyg-1*^{RNAi} experiments (Figure 7A).
459
460 Aside from localizing PCH-2 to unattached kinetochores (Nelson et al., 2015), we
461 wondered if CMT-1 was required for any other aspects of PCH-2 regulation. Therefore,
462 we tested whether CMT-1 was necessary for PCH-2's asymmetric enrichment in P_1
463 cells. We quantified PCH-2::GFP fluorescence in prometaphase in the area around
464 chromosomes in both *cmt-1* mutant AB and P_1 cells (Figure 7C). First, we found that
465 PCH-2::GFP fluorescence was slightly higher in AB cells in *cmt-1* mutants than control
466 embryos (Figure 7D). We saw a similar result in our *par-1* RNAi experiments (data not
467 shown), although in both cases these increases were not statistically significant.
468 However, unlike *par-1*^{RNAi} embryos (Gerhold et al., 2018), this increase in PCH-2::GFP
469 was not accompanied by an increase in checkpoint strength (Figure 7B), consistent with
470 our hypothesis that the weaker checkpoint in *cmt-1* AB cells is a consequence of the
471 absence of PCH-2 recruitment at unattached kinetochores (Nelson et al., 2015). Further,
472 when we compared the quantification of PCH-2::GFP fluorescence in *cmt-1* mutant AB
473 and P_1 cells, we did not detect a significant difference between the two cells (Figure 7E),
474 unlike our experiment in control embryos (Figures 6B and C), indicating that CMT-1
475 contributes to the asymmetric enrichment of PCH-2 in P_1 cells. Thus, it appears that
476 CMT-1 promotes spindle checkpoint strength through two mechanisms: localizing PCH-2

477 to unattached kinetochores and ensuring its enrichment around mitotic chromosomes in
478 germline precursor cells.
479
480 **DISCUSSION**
481
482 The role of PCH-2, and its mammalian ortholog TRIP13, in the spindle checkpoint has
483 been enigmatic. Originally identified as a checkpoint silencing factor (Alfieri et al., 2018,
484 Brulotte et al., 2017, Eytan et al., 2014, Miniowitz-Shemtov et al., 2015, Wang et al.,
485 2014, Ye et al., 2015), more recent evidence also indicates a role in promoting the
486 checkpoint response (Ma & Poon, 2016, Ma & Poon, 2018, Nelson et al., 2015, Yost et
487 al., 2017). It's clear that the reliance on PCH-2/TRIP13 in checkpoint activation likely
488 reflects the relative levels and availability of O-Mad2 (Ma & Poon, 2018). We show here
489 that PCH-2, likely in its role regulating O-Mad2 availability, specifically at and near
490 unattached kinetochores, also controls checkpoint strength, providing an unanticipated
491 mechanism to explain its regulation (Figure 8). We propose that this role in checkpoint
492 strength is particularly important in large cells, such as oocytes and cells in early
493 embryos, as well as cells that give rise to immortal germ cells.
494
495 Our model assumes that two cell embryos have a significant amount of O-Mad2
496 available, even when PCH-2 function is lost (Figure 8), unlike what is reported in
497 mammalian cells (Ma & Poon, 2016). Given that this is a developmental system in which
498 embryos have only undergone a single mitotic division before we perform our assays,
499 we propose that O-Mad2 is not limiting in very early embryos, even in *pch-2* null
500 mutants. In this way, *C. elegans* two-cell embryos would be analogous to mammalian
501 cells undergoing cell division soon after acute depletion of TRIP13 (Ma & Poon, 2018).
502 Unfortunately, we were unable to directly probe O-Mad2 concentration or its availability

503 at or near unattached kinetochores in small *ani-2*^{RNAi} embryos or germline precursor
504 cells. However, we think that several pieces of correlative data support this hypothesis:
505 PCH-2's characterized biochemical activity converts C-Mad2 to O-Mad2 (Alfieri et al.,
506 2018, Brulotte et al., 2017, Ye et al., 2015); the delay we observe in small *pch-2;ani-*
507 *2*^{RNAi}*;zyg-1*^{RNAi} embryos is checkpoint dependent (Figure S1B); as cells are genetically
508 manipulated to become smaller, robust checkpoint strength depends on Mad2 dosage
509 (Figure 2C); GFP::MAD-2 localization is restored to unattached kinetochores in small
510 *pch-2;ani-2*^{RNAi}*;zyg-1*^{RNAi} embryos (Figures 2D and E); and *pch-2* and *mad-2* mutant
511 alleles genetically interact (data not shown), indicating a close functional relationship
512 between these two genes during embryogenesis.
513
514 Another prediction of our model is that overexpression of Mad2 should also make PCH-2
515 dispensable for spindle checkpoint activation. We've shown that subtle elevations of
516 Mad2 protein levels cannot suppress the requirement for PCH-2 in two-cell embryos
517 (Nelson et al., 2015). Unfortunately, more dramatic overexpression experiments are
518 technically difficult in *C. elegans*. Further, it's likely that strong overexpression of Mad2 in
519 *C. elegans* embryos will delay normal mitosis, consistent with similar findings in
520 mammalian cells (Marks, Thomas et al., 2017) and budding yeast (Mariani, Chiroli et al.,
521 2012). In this way, PCH-2's function may provide a useful buffer: Since Mad2 protein
522 levels may need to stay within a narrow range to allow normal mitotic timing, PCH-2's
523 localization at and near unattached kinetochores provide a mechanism to increase O-
524 Mad2's local concentration to promote effective and efficient signaling during checkpoint
525 activation.
526
527 Despite our findings that PCH-2 becomes dispensable for spindle checkpoint activation
528 as two-cell embryos are experimentally induced to decrease in volume, PCH-2 remains

529 essential for the spindle checkpoint as AB cells normally decrease in volume during
530 embryogenesis (Figure 4). This may reflect that O-Mad2 eventually does become
531 limiting in cells of the AB lineage with successive divisions after the two-cell stage and
532 thus, there is a greater reliance on PCH-2 function. Moreover, it may also suggest that
533 relative levels of O-Mad2 and C-Mad2 are more stringently regulated as embryonic
534 development progresses and the multi-cellular embryo becomes more complex. This
535 possibility is supported by our finding that PCH-2 regulates normal cell cycle timing in P_1
536 cells, but not AB cells (Figure 5C), which implies that variations in O-Mad2/C-Mad2
537 ratios influence normal mitotic timing in cells with specific developmental fates. In
538 addition, unlike the nuclei of two-cell embryos treated with *ani-2*^{RNAi} (Figure S2), nuclear
539 volume scales with cell volume during embryogenesis (Gerhold et al., 2018). Therefore,
540 the concentration of Mad2 may not necessarily increase as cell size decreases in cells of
541 the developing embryo, making direct comparisons between small cells obtained by *ani-*
542 *2*^{RNAi} treatment and small cells resulting from normal embryogenesis challenging.
543
544 Our experiments identify CMT-1, the *C. elegans* ortholog of mammalian p31^{comet}, as an
545 important regulator of PCH-2 function and, as a result, checkpoint strength. In addition to
546 its requirement in facilitating PCH-2's ability to interact with its substrate, Mad2 (Alfieri et
547 al., 2018, Brulotte et al., 2017, Miniowitz-Shemtov et al., 2015, Ye et al., 2015), CMT-1
548 localizes PCH-2 to unattached kinetochores (Nelson et al., 2015) and promotes PCH-2's
549 enrichment in P_1 cells (Figure 7). We propose that both of these roles contribute to
550 checkpoint strength. In large AB cells, CMT-1 ensures PCH-2's presence at unattached
551 kinetochores, increasing the local concentration of O-Mad2 and driving the production of
552 soluble C-Mad2 and MCC (Figure 8A). In P_1 cells, the combination of PCH-2's
553 localization at kinetochores and its enrichment around chromosomes and near
554 unattached kinetochores produces a checkpoint stronger than somatic cells (Figure 8C).

555 It's striking that AB cells, in which there is more PCH-2 (Figure 7D), and P_1 cells, which
556 are slightly smaller than AB cells, exhibit similar checkpoint strength when CMT-1 is
557 absent (Figure 7B). This indicates that even these cells depend on PCH-2 to be present
558 at unattached kinetochores to increase the local concentration of O-Mad2 and promote
559 checkpoint strength.
560
561 P_1 cells in both *pch-2;ani-2*^{RNAi}*;zyg-1*^{RNAi} and *cmt-1;ani-2*^{RNAi}*;zyg-1*^{RNAi} mutants show
562 faster cell cycle timing than similarly sized AB cells of the same genotype (Figures 5B
563 and 7A). However, only *pch-2* mutants significantly affect cell cycle timing in unperturbed
564 P_1 cells, (Figure 5C); P_1 cells in *cmt-1* and *mad-1* mutants show accelerated cell cycle
565 timing but this is not significantly faster than control (Figures 5C and 7B). Given the
566 rapidity of cell cycles in these early embryos, it's possible that *ani-2*^{RNAi}*;zyg-1*^{RNAi}
567 experiments provide greater sensitivity to observe subtle accelerations in cell cycle
568 timing and that some subset of spindle checkpoint components, including PCH-2, CMT-
569 1, MAD-1 and MAD-2 regulate normal cell cycle timing in germline precursor cells,
570 similar to the role of MAD-1 and MAD-2 in germline mitotic nuclei (Gerhold et al., 2015).
571 An alternative hypothesis that we do not favor is that only PCH-2 regulates cell cycle
572 timing in P_1 cells, in a mechanism independent of other spindle checkpoint proteins.
573
574 Evolutionary analysis across phyla have revealed a close co-evolutionary relationship
575 between PCH-2 and its orthologs and HORMA domain containing proteins, including
576 CMT-1 and Mad2 (van Hooff, Tromer et al., 2017, Vleugel, Hoogendoorn et al., 2012).
577 However, some organisms that rely on the templated conversion of O-Mad2 to C-Mad2
578 to assemble the MCC, such as budding and fission yeasts (Chao, Kulkarni et al., 2012,
579 Nezi, Rancati et al., 2006) either don't express their PCH-2 ortholog during mitosis
580 (budding yeast) (San-Segundo & Roeder, 1999) or don't have a PCH-2 ortholog in their

581 genome (fission yeast) (Wu & Burgess, 2006). This is potentially explained by cell
582 volume: Both budding and fission yeasts are two orders of magnitude smaller than
583 mammalian cells and *C. elegans* embryos. They also undergo closed mitosis, in which
584 the nuclear envelope does not break down, providing an additional opportunity to
585 concentrate factors required for mitosis. We propose that recruiting O-Mad2 to
586 unattached kinetochores may not present as great a challenge in these significantly
587 smaller cells, making a factor required to increase the local concentration of O-Mad2 at
588 unattached kinetochores unnecessary.
589
590 An obvious question our experiments raise is how PCH-2 is enriched in P_1 cells.
591 Germline precursor cells are transcriptionally silent until gastrulation (Seydoux, Mello et
592 al., 1996) and sequencing of mRNA in early embryos shows that both CMT-1 and PCH-
593 2 mRNA are not enriched in germline precursor cells (Tintori et al., 2016), indicating that
594 enrichment of PCH-2 is likely to occur at the level of protein regulation. Understanding
595 this regulation, its control by developmental events and its effect on the relative levels of
596 O-Mad2 and C-Mad2 in different cell types promises to be an exciting area of
597 investigation.
598
599 **MATERIALS AND METHODS**
600
601 **Worms strains**
602 The *C. elegans* Bristol N2 (Brenner, 1974) was used as the wild-type strain. Most strains
603 were maintained at 20°C, except for *zyg-1(or297)* strains, which were maintained at
604 15°C. See Table S1 for the list of all the strains used in this study.
605
606 **Immunostaining**

607 Immunostaining was performed on adult worms 48h after L4, as described in (Bhalla &
608 Dernburg, 2005). The antibodies used were rabbit anti-MAD-2 (1/500; (Essex et al.,
609 2009) and mouse anti-MAb414 (1/400; (Davis & Blobel, 1986). Secondary antibodies
610 were Alexa Fluor 488 anti-rabbit (Invitrogen) and Cy3 anti-mouse (Jackson
611 ImmunoResearch Laboratories, Inc.) diluted at 1:500. Antibody against MAD-2 was a gift
612 from A. Desai (Ludwig Institute/University of California, San Diego, La Jolla, CA).
613
614 Images were acquired on a DeltaVision Personal DV microscope (GE Healthcare)
615 equipped with a 100× NA 1.40 oil-immersion objective (Olympus), a short ARC xenon
616 lamp (GE Healthcare) and using a CoolSNAP charge-coupled camera (Roper Scientific).
617 Z-stacks were collected at 0.2 μm Z-spacing and processed by constrained, iterative
618 deconvolution. Imaging, image scaling, and analysis were performed using functions in
619 the softWoRx software package (GE Healthcare). Projections were calculated by a
620 maximum intensity algorithm. Composite images were assembled and some false
621 coloring was performed with Fiji.
622
623 **Live imaging of two-cell embryos**
624 For live imaging of two-cell embryos, worms were dissected on glass coverslips in egg
625 buffer and then mounted on 2% agar pads. Images were acquired every 1 minute or 20
626 seconds on a DeltaVision Personal DV microscope as described in the previous section;
627 except that the distance between two planes was 2 μm. Mitotic timing was measured
628 from NEBD to OCC as described in (Nelson et al., 2015). Cell volumes were measured
629 as described in (Galli & Morgan, 2016). To measure the nuclear area, a sum projection
630 of the embryo was generated 1 minute before chromosomes began to condense and the
631 area was measured with Fiji (Figure S2A).
632

633 **Live imaging of embryogenesis**

634 After treatment with *perm-1*^{RNAi} (see below), worms were dissected onto a coverslip with
635 egg salt buffer (118 mM NaCl, 48 mM KCl) supplemented with 10 mM PIPES pH 7.3, 1
636 mM ATP and 10 mM sucrose. Embryos and adult carcasses were transferred into a well
637 of an 8-well plate (ibidi 1 µ-Slide 8 Well Glass bottom) that had been freshly coated with
638 0.1% Poly-L-Lysine solution (Sigma P8920) and extensively washed. Time-lapse videos
639 were acquired with a Solamere spinning disk confocal system piloted by µManager
640 software (Edelstein, Tsuchida et al., 2014) and equipped with a Yokogawa CSUX-1 scan
641 head, a Nikon (Garden City, NY) TE2000-E inverted stand, a Hamamatsu ImageEM ×2
642 camera, LX/MAS 489 nm and LS/MAS 561 nm laser, and Plan Apo ×60/1.4 numerical
643 aperture oil objective. Acquisition times per frame were 50 ms using 5% of the lasers
644 power for both channels, and images were obtained as stacks of planes at 2 µm
645 intervals taken every 1 minute. Nocodazole was added from a 5X stock to a final
646 concentration of 50 µM after the first time point. Mitotic timing was measured from NEBD
647 to DECON as described in (Essex et al., 2009).

648

649 To image embryogenesis in *zyg-1(or297)* mutants, images were generated under the
650 same conditions as previously described for the live imaging of two-cell embryos with a
651 few modifications: Images were acquired every 20 seconds on a DeltaVision Personal
652 DV microscope in a room heated to 26°C. Mitotic timing was measured from NEBD to
653 DECON as described in (Essex et al., 2009).

654

655 **Quantification of fluorescence intensity**

656 To quantify GFP::MAD-2 and PCH-2::GFP levels, images were generated under the
657 same conditions as previously described for the live imaging of two-cell embryos with a
658 few modifications: only the nucleus was imaged, the interval between the four planes

659 was 1 µm and images were collected every 20 seconds. Quantification of fluorescence
660 at kinetochores was performed in Fiji as described in (Moyle, Kim et al., 2014, Nelson et
661 al., 2015) and fluorescence in the cytoplasm as described in (Galli & Morgan, 2016). In
662 some of our movies, identifying a clear metaphase plate was more difficult in AB than P_1
663 cells. Therefore, to ensure that we were quantifying PCH-2::GFP fluorescence around
664 mitotic chromosomes at the same stage in mitosis in these two cell types, PCH-2::GFP
665 was quantified in frames that were normalized relative to NEBD and mitotic exit. Sum
666 intensity projections were generated and fluorescence in the area around mitotic
667 chromosomes was measured in Fiji. Background fluorescence was measured in a 30
668 pixel band around this "cloud" and subtracted from the initial fluorescence intensity to
669 determine the final fluorescence value. To measure the cell volume, one Z-stack of the
670 entire cell was taken at NEBD at 2 µm Z-spacing.
671
672 **Feeding RNA interference (RNAi)**
673 *C. elegans* strains were fed HT115 bacteria expressing the desired dsRNA after IPTG
674 induction. Bacterial strains containing RNAi vectors were cultured overnight at 37°C,
675 centrifuged, and the pellet was resuspended in 1/50 of the original volume. 100 µl of
676 concentrated culture was spotted onto a nematode growth medium (NGM) plate
677 containing 1 mM IPTG and 50 µg/µl of kanamycin or carbenicillin and the plate was
678 incubated overnight at 37°C.
679
680 For *ani-2* RNAi, gravid adults were bleached onto the RNAi plate and their progeny was
681 allowed to develop at 20°C during 2.5 days. Then, L4s were transferred to a fresh plate
682 containing OP50 or *zyg-1* RNAi bacteria.
683

684 For *zyg-1* RNAi, L4s were transferred (from an OP50 or *ani-2* RNAi plate) onto a *zyg-1*
685 RNAi plate and cultured 1.5 days at 20°C.
686
687 For *perm-1* RNAi, young adults (8h post L4) were incubated onto *perm-1* RNAi plates for
688 16-20 hours at 15°C.
689
690 For *par-1* and *gpr-1/2* RNAi, gravid adults were bleached onto control RNAi (L4440)
691 plates and their progeny were allowed to develop at 15°C for 3 days. L4s were then
692 transferred onto *par-1, gpr-1/2* RNAi or control RNAi plates and incubated at 15°C for 3
693 days.
694
695 **Statistical Analysis**
696 Linear regression analysis and assessing significance of this data (Figures 1C, 2C, 3A,
697 5A, 5B, 7A, S1C, S1D, S3A, S4) was performed using GrapPad Prism version 6 for
698 Macintosh. For all other data, significance was assessed by performing t-tests (Figures
699 1D, 2E, 3C, 3D, 3E, 4A, 4B, 5C, 6A, 6C, 6E, 7B, 7D, 7E, S5B, S5D, S6B and S7C). In all
700 graphs, a * indicates a p value < 0.05, ** indicates a p value < 0.01 and *** a p value <
701 0.0001.
702
703 **ACKNOWLEDGEMENTS**
704
705 We would like to thank Arshad Desai, Karen Oegema, Susan Strome and David Morgan
706 for valuable strains and reagents. This work was supported by the NIH (grant numbers
707 T32GM008646 [C.R.N. and A.R.] and R01GM097144 [N.B.]). Some strains were
708 provided by the CGC, which is funded by NIH Office of Research Infrastructure
709 Programs (P40 OD010440).

CONTRIBUTIONS

Conceptualization and Methodology, L.D., A.E.R., C.R.N. and N.B.; Investigation, L.D., A.E.R., and C.R.N.; Writing - Original Draft, L.D. and N.B.; Writing - Review & Editing, L.D., A.E.R., C.R.N. and N.B.; Supervision and Funding Acquisition, N.B.

COMPETING INTERESTS

The authors declare no competing interests.

720 **REFERENCES**

721 Alfieri C, Chang L, Barford D (2018) Mechanism for remodelling of the cell cycle
722 checkpoint protein MAD2 by the ATPase TRIP13. Nature 559: 274-278
723 Aravind L, Koonin EV (1998) The HORMA domain: a common structural denominator in
724 mitotic checkpoints, chromosome synapsis and DNA repair. Trends Biochem Sci 23:
725 284-6
726 Bhalla N, Dernburg AF (2005) A conserved checkpoint monitors meiotic chromosome
727 synapsis in Caenorhabditis elegans. Science 310: 1683-6
728 Bohr T, Nelson CR, Klee E, Bhalla N (2015) Spindle assembly checkpoint proteins
729 regulate and monitor meiotic synapsis in C. elegans. J Cell Biol 211: 233-42
730 Brenner S (1974) The genetics of Caenorhabditis elegans. Genetics 77: 71-94
731 Brulotte ML, Jeong BC, Li F, Li B, Yu EB, Wu Q, Brautigam CA, Yu H, Luo X (2017)
732 Mechanistic insight into TRIP13-catalyzed Mad2 structural transition and spindle
733 checkpoint silencing. Nat Commun 8: 1956
734 Carvalho A, Olson SK, Gutierrez E, Zhang K, Noble LB, Zanin E, Desai A, Groisman A,
735 Oegema K (2011) Acute drug treatment in the early C. elegans embryo. PLoS One 6:
736 e24656
737 Chao WC, Kulkarni K, Zhang Z, Kong EH, Barford D (2012) Structure of the mitotic
738 checkpoint complex. Nature 484: 208-13
739 Chen RH, Shevchenko A, Mann M, Murray AW (1998) Spindle checkpoint protein
740 Xmad1 recruits Xmad2 to unattached kinetochores. J Cell Biol 143: 283-95
741 Chen RH, Waters JC, Salmon ED, Murray AW (1996) Association of spindle assembly
742 checkpoint component XMAD2 with unattached kinetochores. Science 274: 242-6
743 Collin P, Nashchekina O, Walker R, Pines J (2013) The spindle assembly checkpoint
744 works like a rheostat rather than a toggle switch. Nat Cell Biol 15: 1378-85

745 Colombo K, Grill SW, Kimple RJ, Willard FS, Siderovski DP, Gonczy P (2003)
746 Translation of polarity cues into asymmetric spindle positioning in Caenorhabditis
747 elegans embryos. Science 300: 1957-61
748 Davis LI, Blobel G (1986) Identification and characterization of a nuclear pore complex
749 protein. Cell 45: 699-709
750 De Antoni A, Pearson CG, Cimini D, Canman JC, Sala V, Nezi L, Mapelli M, Sironi L,
751 Faretta M, Salmon ED, Musacchio A (2005) The Mad1/Mad2 complex as a template for
752 Mad2 activation in the spindle assembly checkpoint. Current biology : CB 15: 214-25
753 Defachelles L, Hainline SG, Menant A, Lee LA, Karess RE (2015) A maternal effect
754 rough deal mutation suggests that multiple pathways regulate Drosophila RZZ
755 kinetochore recruitment. J Cell Sci 128: 1204-16
756 Dick AE, Gerlich DW (2013) Kinetic framework of spindle assembly checkpoint
757 signalling. Nat Cell Biol 15: 1370-7
758 Edelstein AD, Tsuchida MA, Amodaj N, Pinkard H, Vale RD, Stuurman N (2014)
759 Advanced methods of microscope control using muManager software. J Biol Methods 1
760 Essex A, Dammermann A, Lewellyn L, Oegema K, Desai A (2009) Systematic analysis
761 in Caenorhabditis elegans reveals that the spindle checkpoint is composed of two largely
762 independent branches. Mol Biol Cell 20: 1252-67
763 Eytan E, Wang K, Miniowitz-Shemtov S, Sitry-Shevah D, Kaisari S, Yen TJ, Liu ST,
764 Hershko A (2014) Disassembly of mitotic checkpoint complexes by the joint action of the
765 AAA-ATPase TRIP13 and p31(comet). Proc Natl Acad Sci U S A 111: 12019-24
766 Fava LL, Kaulich M, Nigg EA, Santamaria A (2011) Probing the in vivo function of
767 Mad1:C-Mad2 in the spindle assembly checkpoint. EMBO J 30: 3322-36
768 Galli M, Morgan DO (2016) Cell Size Determines the Strength of the Spindle Assembly
769 Checkpoint during Embryonic Development. Dev Cell 36: 344-52

770 Gerhold AR, Poupart V, Labbe JC, Maddox PS (2018) Spindle assembly checkpoint
771 strength is linked to cell fate in the Caenorhabditis elegans embryo. Mol Biol Cell 29:
772 1435-1448
773 Gerhold AR, Ryan J, Vallee-Trudeau JN, Dorn JF, Labbe JC, Maddox PS (2015)
774 Investigating the regulation of stem and progenitor cell mitotic progression by in situ
775 imaging. Curr Biol 25: 1123-34
776 Gotta M, Dong Y, Peterson YK, Lanier SM, Ahringer J (2003) Asymmetrically distributed
777 C. elegans homologs of AGS3/PINS control spindle position in the early embryo. Curr
778 Biol 13: 1029-37
779 Guo S, Kemphues KJ (1995) par-1, a gene required for establishing polarity in C.
780 elegans embryos, encodes a putative Ser/Thr kinase that is asymmetrically distributed.
781 Cell 81: 611-20
782 Kyogoku H, Kitajima TS (2017) Large Cytoplasm Is Linked to the Error-Prone Nature of
783 Oocytes. Dev Cell 41: 287-298 e4
784 Lawrence KS, Chau T, Engebrecht J (2015) DNA damage response and spindle
785 assembly checkpoint function throughout the cell cycle to ensure genomic integrity.
786 PLoS Genet 11: e1005150
787 Li Y, Benezra R (1996) Identification of a human mitotic checkpoint gene: hsMAD2.
788 Science 274: 246-8
789 Luo X, Tang Z, Rizo J, Yu H (2002) The Mad2 spindle checkpoint protein undergoes
790 similar major conformational changes upon binding to either Mad1 or Cdc20. Mol Cell 9:
791 59-71
792 Luo X, Tang Z, Xia G, Wassmann K, Matsumoto T, Rizo J, Yu H (2004) The Mad2
793 spindle checkpoint protein has two distinct natively folded states. Nat Struct Mol Biol 11:
794 338-45

795 Ma HT, Poon RY (2016) TRIP13 Regulates Both the Activation and Inactivation of the
796 Spindle-Assembly Checkpoint. Cell Rep 14: 1086-99
797 Ma HT, Poon RYC (2018) TRIP13 Functions in the Establishment of the Spindle
798 Assembly Checkpoint by Replenishing O-MAD2. Cell Rep 22: 1439-1450
799 Maddox AS, Habermann B, Desai A, Oegema K (2005) Distinct roles for two C. elegans
800 anillins in the gonad and early embryo. Development 132: 2837-48
801 Mariani L, Chiroli E, Nezi L, Muller H, Piatti S, Musacchio A, Ciliberto A (2012) Role of
802 the Mad2 dimerization interface in the spindle assembly checkpoint independent of
803 kinetochores. Curr Biol 22: 1900-8
804 Marks DH, Thomas R, Chin Y, Shah R, Khoo C, Benezra R (2017) Mad2
805 Overexpression Uncovers a Critical Role for TRIP13 in Mitotic Exit. Cell Rep 19: 1832-
806 1845
807 Meraldi P, Draviam VM, Sorger PK (2004) Timing and checkpoints in the regulation of
808 mitotic progression. Dev Cell 7: 45-60
809 Miniowitz-Shemtov S, Eytan E, Kaisari S, Sitry-Shevah D, Hershko A (2015) Mode of
810 interaction of TRIP13 AAA-ATPase with the Mad2-binding protein p31comet and with
811 mitotic checkpoint complexes. Proc Natl Acad Sci U S A 112: 11536-40
812 Moyle MW, Kim T, Hattersley N, Espeut J, Cheerambathur DK, Oegema K, Desai A
813 (2014) A Bub1-Mad1 interaction targets the Mad1-Mad2 complex to unattached
814 kinetochores to initiate the spindle checkpoint. J Cell Biol 204: 647-57
815 Nelson CR, Hwang T, Chen PH, Bhalla N (2015) TRIP13PCH-2 promotes Mad2
816 localization to unattached kinetochores in the spindle checkpoint response. J Cell Biol
817 211: 503-16
818 Nezi L, Rancati G, De Antoni A, Pasqualato S, Piatti S, Musacchio A (2006)
819 Accumulation of Mad2-Cdc20 complex during spindle checkpoint activation requires

820 binding of open and closed conformers of Mad2 in Saccharomyces cerevisiae. J Cell
821 Biol 174: 39-51
822 Nystul TG, Goldmark JP, Padilla PA, Roth MB (2003) Suspended animation in C.
823 elegans requires the spindle checkpoint. Science 302: 1038-41
824 O'Connell KF, Caron C, Kopish KR, Hurd DD, Kemphues KJ, Li Y, White JG (2001) The
825 C. elegans zyg-1 gene encodes a regulator of centrosome duplication with distinct
826 maternal and paternal roles in the embryo. Cell 105: 547-58
827 O'Rourke SM, Carter C, Carter L, Christensen SN, Jones MP, Nash B, Price MH,
828 Turnbull DW, Garner AR, Hamill DR, Osterberg VR, Lyczak R, Madison EE, Nguyen
829 MH, Sandberg NA, Sedghi N, Willis JH, Yochem J, Johnson EA, Bowerman B (2011) A
830 survey of new temperature-sensitive, embryonic-lethal mutations in C. elegans: 24
831 alleles of thirteen genes. PLoS One 6: e16644
832 Rodriguez-Bravo V, Maciejowski J, Corona J, Buch HK, Collin P, Kanemaki MT, Shah
833 JV, Jallepalli PV (2014) Nuclear pores protect genome integrity by assembling a
834 premitotic and Mad1-dependent anaphase inhibitor. Cell 156: 1017-31
835 Rose L, Gonczy P (2014) Polarity establishment, asymmetric division and segregation of
836 fate determinants in early C. elegans embryos. WormBook: 1-43
837 Rosenberg SC, Corbett KD (2015) The multifaceted roles of the HORMA domain in
838 cellular signaling. J Cell Biol 211: 745-55
839 San-Segundo PA, Roeder GS (1999) Pch2 links chromatin silencing to meiotic
840 checkpoint control. Cell 97: 313-24
841 Seydoux G, Mello CC, Pettitt J, Wood WB, Priess JR, Fire A (1996) Repression of gene
842 expression in the embryonic germ lineage of C. elegans. Nature 382: 713-6
843 Simonetta M, Manzoni R, Mosca R, Mapelli M, Massimiliano L, Vink M, Novak B,
844 Musacchio A, Ciliberto A (2009) The influence of catalysis on mad2 activation dynamics.
845 PLoS Biol 7: e10

846 Sironi L, Mapelli M, Knapp S, De Antoni A, Jeang KT, Musacchio A (2002) Crystal
847 structure of the tetrameric Mad1-Mad2 core complex: implications of a 'safety belt'
848 binding mechanism for the spindle checkpoint. EMBO J 21: 2496-506
849 Sironi L, Melixetian M, Faretta M, Prosperini E, Helin K, Musacchio A (2001) Mad2
850 binding to Mad1 and Cdc20, rather than oligomerization, is required for the spindle
851 checkpoint. EMBO J 20: 6371-82
852 Srinivasan DG, Fisk RM, Xu H, van den Heuvel S (2003) A complex of LIN-5 and GPR
853 proteins regulates G protein signaling and spindle function in C elegans. Genes Dev 17:
854 1225-39
855 Sudakin V, Chan GK, Yen TJ (2001) Checkpoint inhibition of the APC/C in HeLa cells is
856 mediated by a complex of BUBR1, BUB3, CDC20, and MAD2. J Cell Biol 154: 925-36
857 Tintori SC, Osborne Nishimura E, Golden P, Lieb JD, Goldstein B (2016) A
858 Transcriptional Lineage of the Early C. elegans Embryo. Dev Cell 38: 430-44
859 Tipton AR, Wang K, Oladimeji P, Sufi S, Gu Z, Liu ST (2012) Identification of novel
860 mitosis regulators through data mining with human centromere/kinetochore proteins as
861 group queries. BMC Cell Biol 13: 15
862 Vader G (2015) Pch2(TRIP13): controlling cell division through regulation of HORMA
863 domains. Chromosoma 124: 333-9
864 van Hooff JJ, Tromer E, van Wijk LM, Snel B, Kops GJ (2017) Evolutionary dynamics of
865 the kinetochore network in eukaryotes as revealed by comparative genomics. EMBO
866 Rep
867 Vleugel M, Hoogendoorn E, Snel B, Kops GJ (2012) Evolution and function of the mitotic
868 checkpoint. Dev Cell 23: 239-50
869 Wang K, Sturt-Gillespie B, Hittle JC, Macdonald D, Chan GK, Yen TJ, Liu ST (2014)
870 Thyroid hormone receptor interacting protein 13 (TRIP13) AAA-ATPase is a novel
871 mitotic checkpoint-silencing protein. J Biol Chem 289: 23928-37

872 Wu HY, Burgess SM (2006) Two distinct surveillance mechanisms monitor meiotic
873 chromosome metabolism in budding yeast. Curr Biol 16: 2473-9
874 Yang M, Li B, Tomchick DR, Machius M, Rizo J, Yu H, Luo X (2007) p31comet blocks
875 Mad2 activation through structural mimicry. Cell 131: 744-55
876 Ye Q, Rosenberg SC, Moeller A, Speir JA, Su TY, Corbett KD (2015) TRIP13 is a
877 protein-remodeling AAA+ ATPase that catalyzes MAD2 conformation switching. eLife 4
878 Yost S, de Wolf B, Hanks S, Zachariou A, Marcozzi C, Clarke M, de Voer RM, Etemad
879 B, Uijttewaal E, Ramsay E, Wylie H, Elliott A, Picton S, Smith A, Smithson S, Seal S,
880 Ruark E, Houge G, Pines J, Kops G et al. (2017) Biallelic TRIP13 mutations predispose
881 to Wilms tumor and chromosome missegregation. Nat Genet
882

883 **Figure Legends**

884

885 **Figure 1: PCH-2 becomes dispensable for the spindle checkpoint response in**

886 **somatic cells as they decrease in size**

887 (A) Images of control and *ani-2*^{RNAi} two-cell embryos. Scale bar indicates 5 µm. (B)

888 Cartoon of embryos treated with *zyg-1*^{RNAi} or *ani-2*^{RNAi}*;zyg-1*^{RNAi}. (C) Mitotic timing, as

889 measured from nuclear envelope breakdown (NEBD) to the onset of cortical contractility

890 (OCC), in AB cells of control, *pch-2* and *mad-1* mutant embryos plotted against cell

891 volume. Lines represent regression analysis for each set of data. (D) Data from (C)

892 partitioned into three categories: wild-type sized embryos (more than 5 x 10^3 µm^3),

893 medium sized embryos (between 3.5 x 10^3 µm^3 and 5 x 10^3 µm^3) and small embryos

894 (less than 3.5 x 10^3 µm^3). Error bars are S.E.M. In all graphs, a * indicates a p value <

895 0.05, ** indicates a p value < 0.01 and *** a p value < 0.0001.

896

897 **Figure 2: PCH-2 becomes dispensable for MAD-2 recruitment at unattached**

898 **kinetochores in somatic cells as they decrease in size**

899 (A) Immunostaining of MAD-2 and nuclear pore complex components (NPCs) shows

900 MAD-2 localized in the nucleus and at the nuclear envelope during interphase. Scale bar

901 indicates 5 µm. (B) Model depicting how a decrease cell volume might result in an

902 increase in the local concentration of O-Mad2 in *ani-2*^{RNAi}*;zyg-1*^{RNAi} embryos, in contrast

903 to *zyg-1*^{RNAi} embryos. (C) Mitotic timing, as measured from nuclear envelope breakdown

904 (NEBD) to the onset of cortical contractility (OCC), in AB cells of control and *mad-2/+*

905 mutant embryos plotted against cell volume. Lines represent regression analysis for

906 each set of data. (D) Cartoon and images of GFP::MAD-2 recruitment to unattached

907 kinetochores in AB cells of small and wild-type sized embryos. Scale bar indicates 1 µm.

908 (E) Quantification of kinetochore bound GFP::MAD-2. Error bars are S.E.M.

909 **Figure 3: PCH-2 is essential for the spindle checkpoint in *ani-2*^{RNAi} small embryos**
910 **treated with nocodazole**
911 (A) Mitotic timing, as measured from nuclear envelope breakdown (NEBD) to
912 decondensation of chromatin (DECON), in AB cells of control, *pch-2* and *san-1* mutant
913 embryos treated with nocodazole plotted against cell volume. Lines represent regression
914 analysis for each set of data. (B) Cartoon and images of PCH-2::GFP localization around
915 mitotic chromosomes in AB cells of two-cell embryos. Scale bar indicates 5 µm. Yellow
916 dashed circle indicates area of PCH-2::GFP fluorescence. (C) Quantification of PCH-
917 2::GFP fluorescence in AB cells with bipolar spindles, monopolar spindles or no
918 spindles. (D) Quantification of area of PCH-2::GFP fluorescence in AB cells with bipolar
919 spindles, monopolar spindles or no spindles. (E) Quantification of integrated density of
920 PCH-2::GFP fluorescence in AB cells with bipolar spindles, monopolar spindles or no
921 spindles. All error bars are S.E.M. NS indicates not significant.
922
923 **Figure 4: PCH-2 is required for the spindle checkpoint response during**
924 **embryogenesis**
925 (A) Mitotic timing, as measured from nuclear envelope breakdown (NEBD) to
926 decondensation of chromatin (DECON), in control, *pch-2* and *san-1* mutant embryos
927 treated with nocodazole at different developmental stages (4- and 16-cell embryos). (B)
928 Mitotic timing in *zyg-1*^{ts} and *pch-2;zyg-1*^{ts} mutant embryos at different developmental
929 stages (2-, 4- and 8-cell embryos). All error bars are S.E.M.
930
931 **Figure 5: PCH-2 is responsible for the stronger spindle checkpoint in the germline**
932 **lineage**
933 Mitotic timing, as measured from nuclear envelope breakdown (NEBD) to the onset of
934 cortical contractility (OCC), in AB and P_1 cells plotted against cell volume in control *ani-*

935 *2^{RNAi};zyg-1^{RNAi}* embryos (A) or *pch-2;ani-2^{RNAi};zyg-1^{RNAi}* (B) embryos. Lines represent
936 regression analysis for each set of data. Data for AB cells in both control and *pch-2*
937 mutants is the same as in Figure 1C. (C) Mitotic timing of AB and P_1 cells in control, *pch-*
938 *2* and *mad-1* mutants during unperturbed divisions. Error bars are S.E.M.
939
940 **Figure 6: PCH-2's enrichment in P_1 cells depends on PAR-1**
941 (A) Mitotic timing of control embryos and embryos expressing PCH-2::GFP during
942 unperturbed divisions or in the presence of monopolar spindles. (B) Cartoon and images
943 of PCH-2::GFP localization around mitotic chromosomes in AB and P_1 cells of two-cell
944 embryos. Scale bar indicates 5 μm. (C) Quantification of PCH-2::GFP fluorescence in
945 AB and P_1 cells. (D) Cartoon and images of PCH-2::GFP localization around mitotic
946 chromosomes in AB and P_1 cells of control RNAi and *par-1^{RNAi}* two-cell embryos. (E)
947 Quantification of PCH-2::GFP fluorescence in AB and P_1 cells of *par-1^{RNAi}* embryos. All
948 error bars are S.E.M. NS indicates not significant.
949
950 **Figure 7: The stronger checkpoint in P_1 cells depends on CMT-1**
951 (A) Mitotic timing, as measured from nuclear envelope breakdown (NEBD) to the onset
952 of cortical contractility (OCC), in AB and P_1 cells plotted against cell volume in *cmt-1;ani-*
953 *2^{RNAi};zyg-1^{RNAi}* embryos. Lines represent regression analysis for each set of data. (B)
954 Mitotic timing of control, *cmt-1* and *mad-1* mutant embryos during unperturbed divisions
955 or in the presence of monopolar spindles. (C) Cartoon and images of PCH-2::GFP
956 localization around mitotic chromosomes in AB and P_1 cells of *cmt-1* mutant embryos.
957 Scale bar indicates 5 μm. (D) Quantification of PCH-2::GFP fluorescence in AB cells of
958 control and *cmt-1* mutant embryos. (E) Quantification of PCH-2::GFP fluorescence in AB
959 and P_1 cells of *cmt-1* mutant embryos. All error bars are S.E.M. NS indicates not
960 significant.

961

962 **Figure 8: Model**

963 (A) A robust spindle checkpoint response in large cells requires the presence of PCH-2
964 at unattached kinetochores to increase the local concentration O-MAD-2 at and near
965 unattached kinetochores. (B) Reducing cell volume of two-cell embryos increases the
966 concentration of O-Mad-2 at and near unattached kinetochores, allowing a checkpoint
967 response in the absence of PCH-2. (C) The enrichment of PCH-2 around mitotic
968 chromosomes in P_1 cells results in a higher production of O-MAD-2, generating a
969 stronger spindle checkpoint response in these cells.

970

971 **Figure S1: Related to Figure 1. The mitotic delay observed in *pch-2;ani-2^{RNAi};zyg-*
972 ***1^{RNAi}* small cells is a spindle checkpoint response.**

973 Cartoon of control and *ani-2^{RNAi}* two-cell embryos (A) and an *ani-2^{RNAi};zyg-1^{RNAi}* two-cell
974 embryo (B). Mitotic timing in AB cells plotted against cell volume, during unperturbed
975 mitosis (C) and in the presence of monopolar spindles. (D). Lines represent regression
976 analysis for each set of data. The regression line of *pch-2;ani-2^{RNAi};zyg-1^{RNAi}* embryos
977 from Figure 1C is indicated by the opaque red line for comparison.

978

979 **Figure S2: Related to Figure 2. Nuclear volume does not scale with cell volume in**
980 ***ani-2^{RNAi}* two-cell embryos.**

981 (A) Images of a large (top) and small (bottom) AB cell of *ani-2^{RNAi}* embryos. The nuclear
982 area is indicated with a dashed yellow line. Scale bar indicates 5 μm. (B) Nuclear area
983 plotted against cell volume.

984

985 **Figure S3: Related to Figure 2: GFP::MAD-2 decreases at unattached kinetochores**
986 **in the AB cells of small *ani-2^{RNAi};zyg-1^{RNAi}* embryos, unlike in *pch-2;ani-2^{RNAi};zyg-***
987 ***1^{RNAi}* embryos.**
988 (A) Quantification of GFP::MAD-2 fluorescence at unattached kinetochores plotted
989 against cell volume in AB cells of control and *pch-2* embryos. Lines represent regression
990 analysis for each set of data. (B) Quantification of GFP::MAD-2 fluorescence around
991 mitotic chromosomes in AB cells of control and *pch-2* embryos plotted against cell
992 volume. (C) Images of MAD-2::GFP in AB cells of control *ani-2^{RNAi};zyg-1^{RNAi}* embryos or
993 *pch-2;ani-2^{RNAi};zyg-1^{RNAi}* embryos. Scale bar indicates 5 μm.
994
995 **Figure S4: Related to Figure 5. PCH-2 is responsible for the stronger spindle**
996 **checkpoint in the germline lineage.**
997 Mitotic timing, as measured from nuclear envelope breakdown (NEBD) to the onset of
998 cortical contractility (OCC), in AB and P_1 cells plotted against cell volume in control *ani-*
999 *2^{RNAi};zyg-1^{RNAi}* embryos or *pch-2;ani-2^{RNAi};zyg-1^{RNAi}* embryos. Lines represent regression
1000 analysis for each set of data.
1001
1002 **Figure S5: Related to Figure 6. There is no difference in the amount of PCH-2::GFP**
1003 **or GFP::MAD-2 recruited to unattached kinetochores in AB and P_1 cells.**
1004 (A) Cartoon and images of PCH-2::GFP recruitment to unattached kinetochores in AB
1005 and P_1 cells of two-cell embryos. Scale bar indicates 1 μm. (B) Quantification of PCH-
1006 2::GFP recruitment at unattached kinetochores in AB and P_1 cells. (C) Cartoon and
1007 images of GFP::MAD-2 recruitment to unattached kinetochores in AB and P_1 cells of
1008 two-cell embryos. Scale bar indicates 1 μm. (D) Quantification of GFP::MAD-2
1009 fluorescence at unattached kinetochores in AB and P_1 cells. All error bars are S.E.M. NS
1010 indicates not significant.

1011

1012 **Figure S6: Related to Figure 6. There is no difference in the amount of PCH-2::GFP**

1013 **in the cytoplasm of AB and P_1 cells.**

1014 (A) Images of AB (left) and P_1 (right) cells after NEBD. Scale bar indicate 5 μm. (B)

1015 Quantification of PCH-2::GFP fluorescence in the cytoplasm of AB and P_1 cells. Error

1016 bars are S.E.M. NS indicates not significant.

1017

1018 **Figure S7: Related to Figure 6. PCH-2's enrichment in P_1 cells depends on GPR-**

1019 **1/2.** (A) Images of two cell embryos treated with control RNAi or RNAi against *gpr-1* and

1020 *gpr-2*. (B) Cartoon and images of PCH-2::GFP localization around mitotic chromosomes

1021 in AB and P_1 cells of control RNAi and *gpr-1/2*^{RNAi} two-cell embryos. Scale bars indicate

1022 5 μm. (C) Quantification of PCH-2::GFP fluorescence in AB and P_1 cells of *gpr-1/2*^{RNAi}

1023 embryos. Error bars are S.E.M.

1024

1025 **Movie legends**

1026

1027 **Video 1**

1028 Mitosis in the AB cell of a wild-type sized control two-cell embryo with monopolar

1029 spindles expressing GFH::PH and mCherry::H2B for visualization of the plasma

1030 membrane and the chromosomes, respectively (strain OD95). The timer starts at NEBD.

1031

1032 **Video 2**

1033 Mitosis in the AB cell of a small control two-cell embryo with monopolar spindles

1034 expressing GFH::PH and mCherry::H2B for visualization of the plasma membrane and

1035 the chromosomes, respectively (strain OD95). The timer starts at NEBD.

1036

1037 **Video 3**

1038 Mitosis in the AB cell of a wild-type sized *pch-2(tm1458)* two-cell embryo with monopolar
1039 spindles expressing GFH::PH and mCherry::H2B for visualization of the plasma
1040 membrane and the chromosomes, respectively (strain BHL575). The timer starts at
1041 NEBD.

1042

1043 **Video 4**

1044 Mitosis in the AB cell of a small *pch-2(tm1458*) two-cell embryo with monopolar spindles
1045 expressing GFH::PH and mCherry::H2B for visualization of the plasma membrane and
1046 the chromosomes, respectively (strain BHL575). The timer starts at NEBD.

1047

1048 **Video 5**

1049 Mitosis in the AB cell of a wild-type sized *mdf-2(tm2190*)/+ two-cell embryo with
1050 monopolar spindles expressing GFH::PH and mCherry::H2B for visualization of the
1051 plasma membrane and the chromosomes, respectively (strain BHL666). The timer starts
1052 at NEBD.

1053

1054 **Video 6**

1055 Mitosis in the AB cell of a small *mdf-2(tm2190*)/+ two-cell embryo with monopolar
1056 spindles expressing GFH::PH and mCherry::H2B for visualization of the plasma
1057 membrane and the chromosomes, respectively (strain BHL666). The timer starts at
1058 NEBD.

1059

1060 **Video 7**

1061 Mitosis in the AB cell of a wild-type sized control two-cell embryo with monopolar
1062 spindles expressing GFH::PH and mCherry::H2B for visualization of the plasma

1063 membrane and the chromosomes, respectively (strain BHL958). The timer starts at
1064 NEBD.
1065
1066 **Video 8**
1067 Mitosis in the AB cell of a small control two-cell embryo with monopolar spindles
1068 expressing GFH::PH and mCherry::H2B for visualization of the plasma membrane and
1069 the chromosomes, respectively (strain BHL958). The timer starts at NEBD.
1070
1071 **Video 9**
1072 Mitosis in a wild-type sized control two-cell embryo after microtubule depolymerization
1073 expressing GFH::tubulin and mCherry::H2B for visualization of the microtubules and the
1074 chromosomes, respectively (strain BHL891). The timer starts at NEBD.
1075
1076 **Video 10**
1077 Mitosis in a wild-type sized *pch-2(tm1458*) two-cell embryo after microtubule
1078 depolymerization expressing GFH::tubulin and mCherry::H2B for visualization of the
1079 microtubules and the chromosomes, respectively (strain BHL892). The timer starts at
1080 NEBD.
1081
1082 **Video 11**
1083 Mitosis in a small *pch-2(tm1458*) two-cell embryo after microtubule depolymerization
1084 expressing GFH::tubulin and mCherry::H2B for visualization of the microtubules and the
1085 chromosomes, respectively (strain BHL892). The timer starts at NEBD.
1086
1087 **Video 12**

1088 Mitosis in the P_1 cell of a wild-type sized control two-cell embryo with monopolar spindles
1089 expressing GFH::PH and mCherry::H2B for visualization of the plasma membrane and
1090 the chromosomes, respectively (strain OD95). The timer starts at NEBD.
1091
1092 **Video 13**
1093 Mitosis in the P_1 cell of a small control two-cell embryo with monopolar spindles
1094 expressing GFH::PH and mCherry::H2B for visualization of the plasma membrane and
1095 the chromosomes, respectively (strain OD95). The timer starts at NEBD.
1096
1097 **Video 14**
1098 Mitosis in the P_1 cell of a wild-type sized *pch-2(tm1458)* two-cell embryo with monopolar
1099 spindles expressing GFH::PH and mCherry::H2B for visualization of the plasma
1100 membrane and the chromosomes, respectively (strain BHL575). The timer starts at
1101 NEBD.
1102
1103 **Video 15**
1104 Mitosis in the P_1 cell of a small *pch-2(tm1458)* two-cell embryo with monopolar spindles
1105 expressing GFH::PH and mCherry::H2B for visualization of the plasma membrane and
1106 the chromosomes, respectively (strain BHL575). The timer starts at NEBD.
1107
1108 **Video 16**
1109 Mitosis in the AB cell of a wild-type sized *cmt-1(ok2879*) two-cell embryo with monopolar
1110 spindles expressing GFH::PH and mCherry::H2B for visualization of the plasma
1111 membrane and the chromosomes, respectively (strain BHL608). The timer starts at
1112 NEBD.
1113

1114 **Video 17**

1115 Mitosis in the AB cell of a small *cmt-1(ok2879*) two-cell embryo with monopolar spindles
1116 expressing GFH::PH and mCherry::H2B for visualization of the plasma membrane and
1117 the chromosomes, respectively (strain BHL608). The timer starts at NEBD.

1118

1119 **Video 18**

1120 Mitosis in the P_1 cell of a wild-type sized *cmt-1(ok2879*) two-cell embryo with monopolar
1121 spindles expressing GFH::PH and mCherry::H2B for visualization of the plasma
1122 membrane and the chromosomes, respectively (strain BHL608). The timer starts at
1123 NEBD.

1124

1125 **Video 19**

1126 Mitosis in the P_1 cell of a small *cmt-1(ok2879*) two-cell embryo with monopolar spindles
1127 expressing GFH::PH and mCherry::H2B for visualization of the plasma membrane and
1128 the chromosomes, respectively (strain BHL608). The timer starts at NEBD.

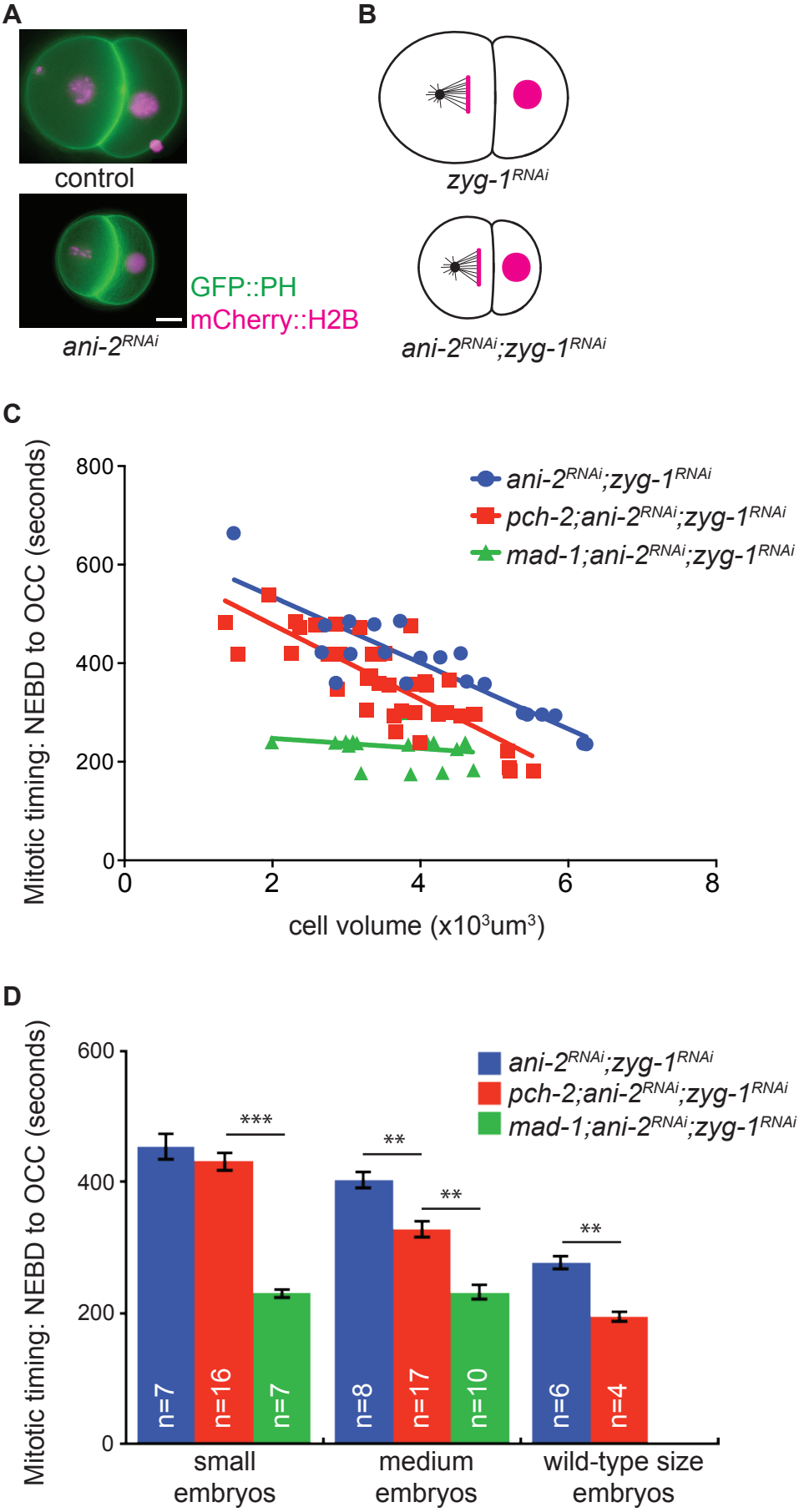
A
control
ani-2RNAi
GFP::PH
mCherry::H2B
B
zyg-1RNAi
ani-2RNAi;zyg-1RNAi
C
Mitotic timing: NEBD to OCC (seconds)
cell volume (x10³um³)
ani-2RNAi;zyg-1RNAi
pch-2;ani-2RNAi;zyg-1RNAi
mad-1;ani-2RNAi;zyg-1RNAi
D
Mitotic timing: NEBD to OCC (seconds)
***
**
**
**
n=7
n=16
n=7
n=8
n=17
n=10
n=6
n=4
small embryos
medium embryos
wild-type size embryos

Défachelles et. al., Figure 2

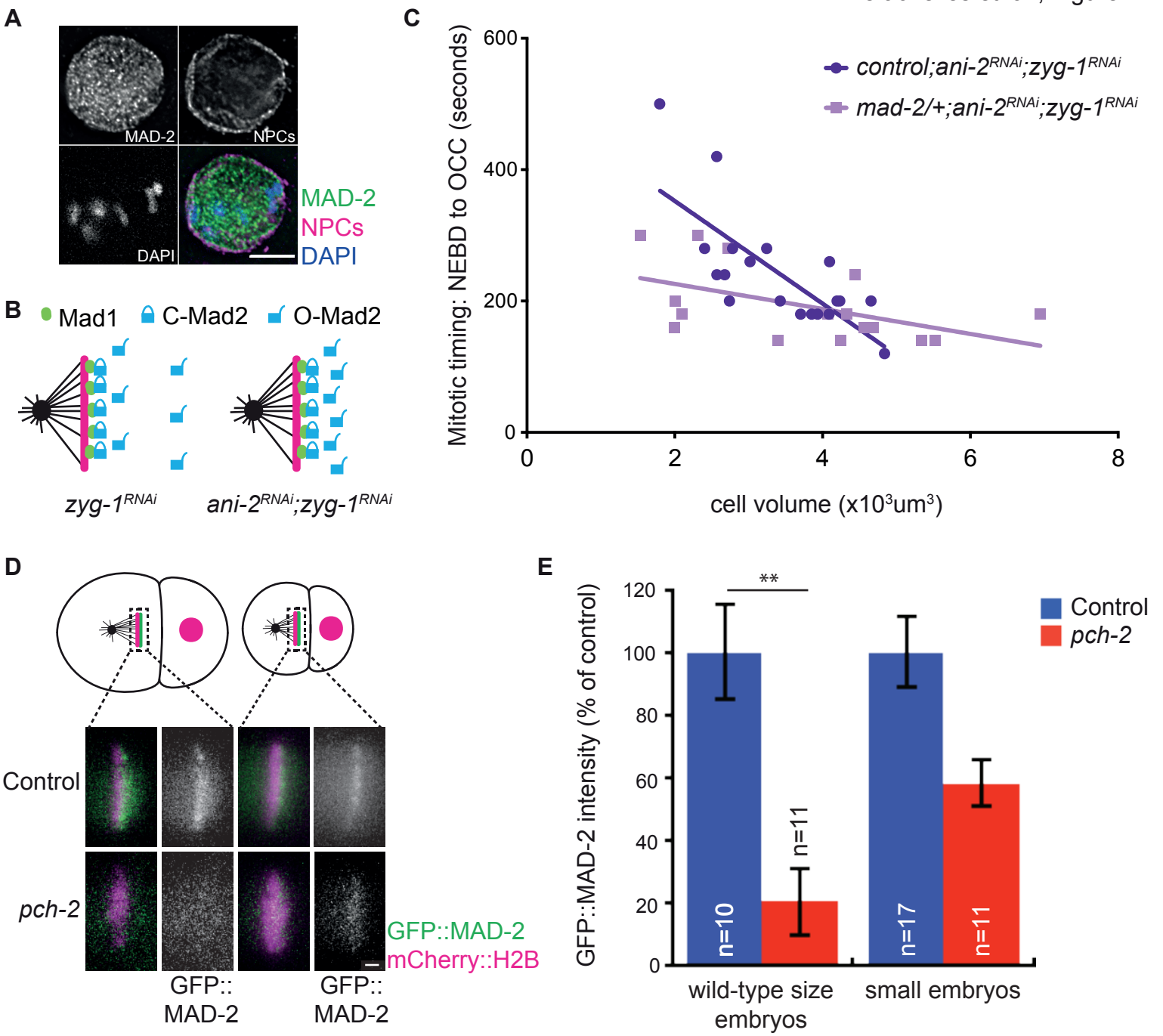

Défachelles et. al., Figure 3

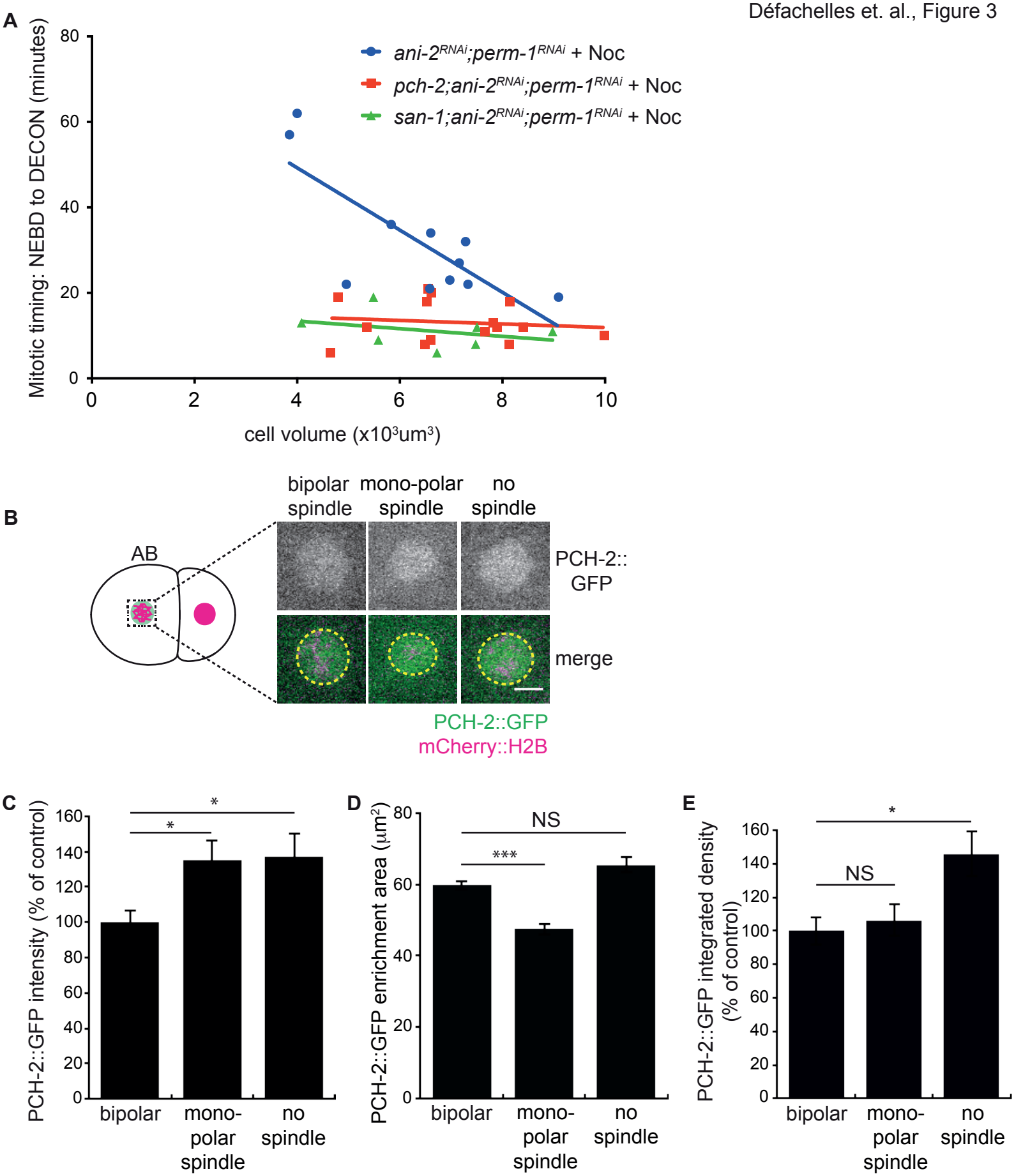

Défachelles et. al., Figure 4

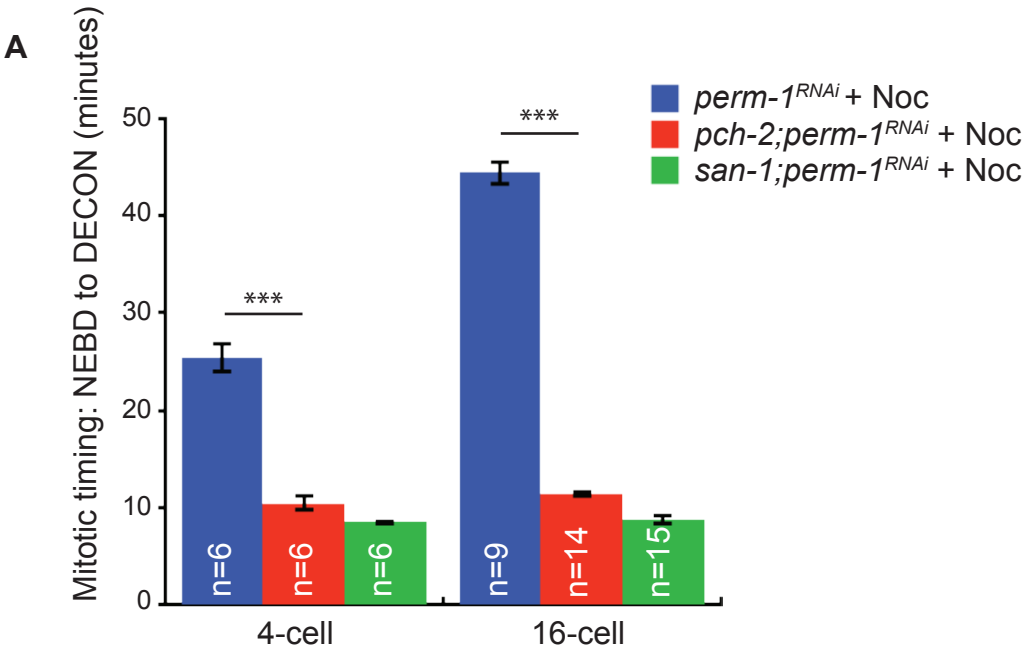

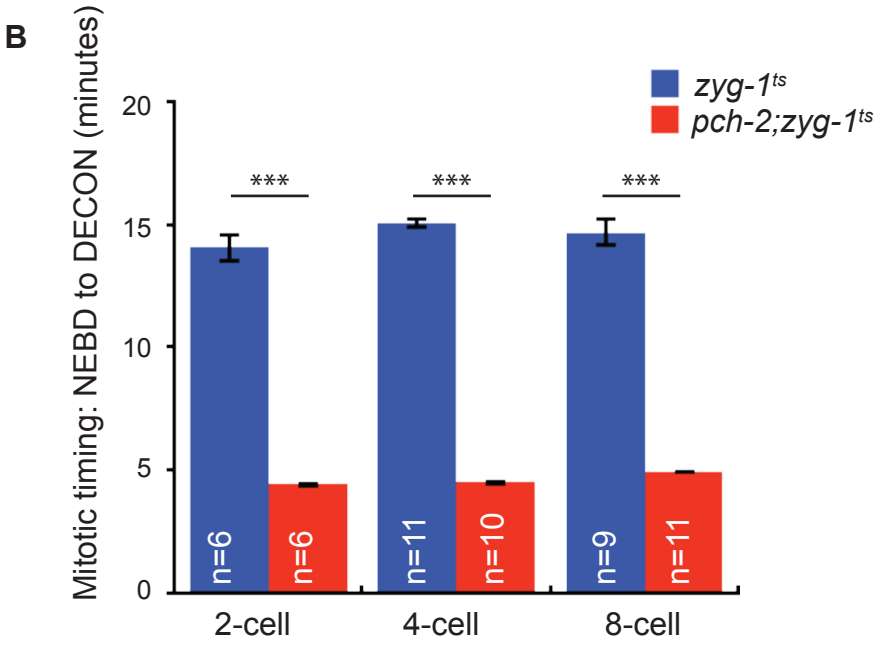

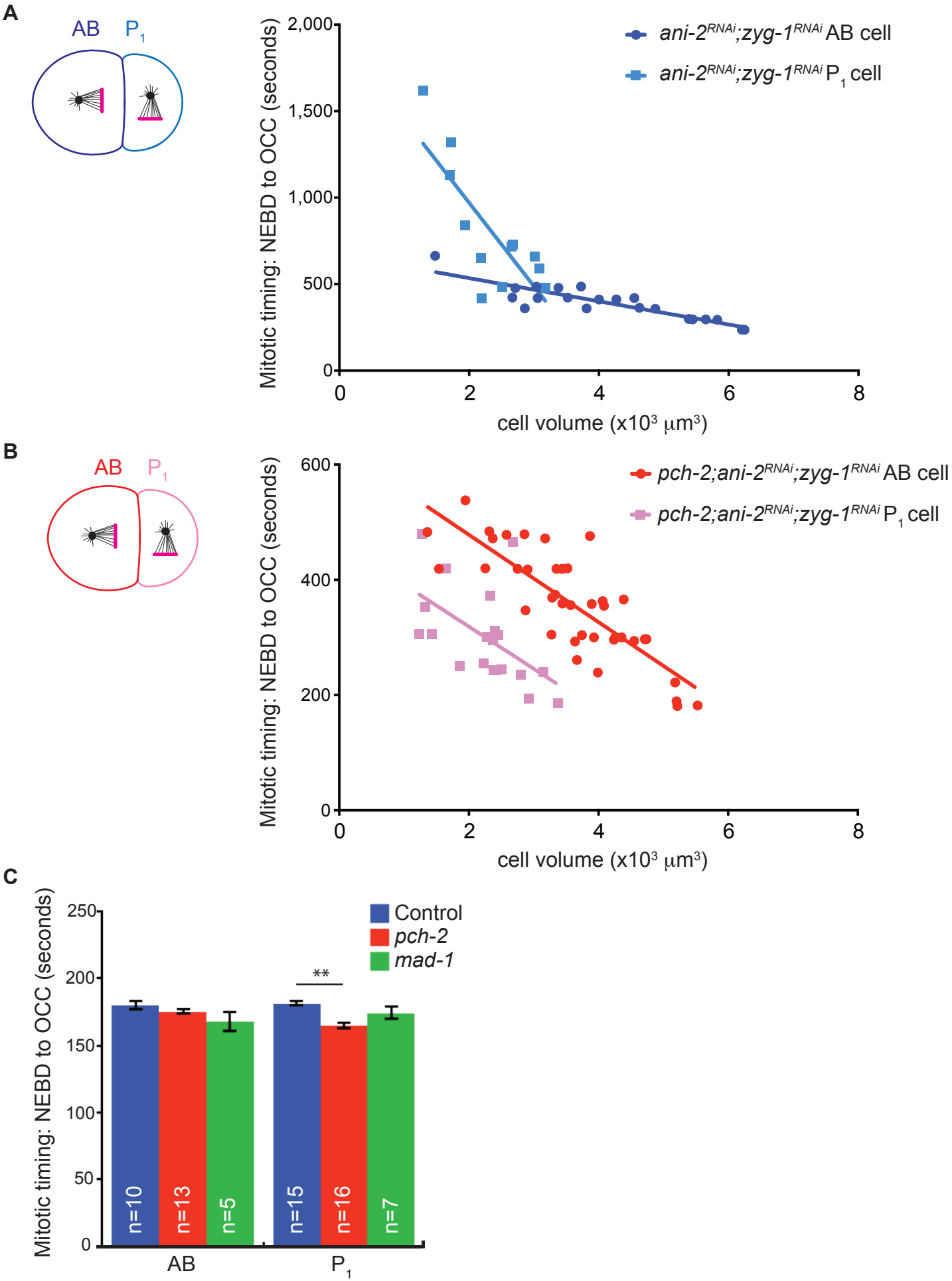
A
AB
P1
Mitotic timing: NEBD to OCC (seconds)
2,000
1,500
1,000
500
0
0
2
4
6
8
cell volume (x10³ µm³)
ani-2RNAi;zyg-1RNAi AB cell
ani-2RNAi;zyg-1RNAi P1 cell
B
AB
P1
Mitotic timing: NEBD to OCC (seconds)
600
400
200
0
0
2
4
6
8
cell volume (x10³ µm³)
pch-2;ani-2RNAi;zyg-1RNAi AB cell
pch-2;ani-2RNAi;zyg-1RNAi P1 cell
C
Mitotic timing: NEBD to OCC (seconds)
250
200
150
100
50
0
Control
pch-2
mad-1
**
n=10
n=13
n=5
n=15
n=16
n=7
AB
P1

Défachelles et. al., Figure 6

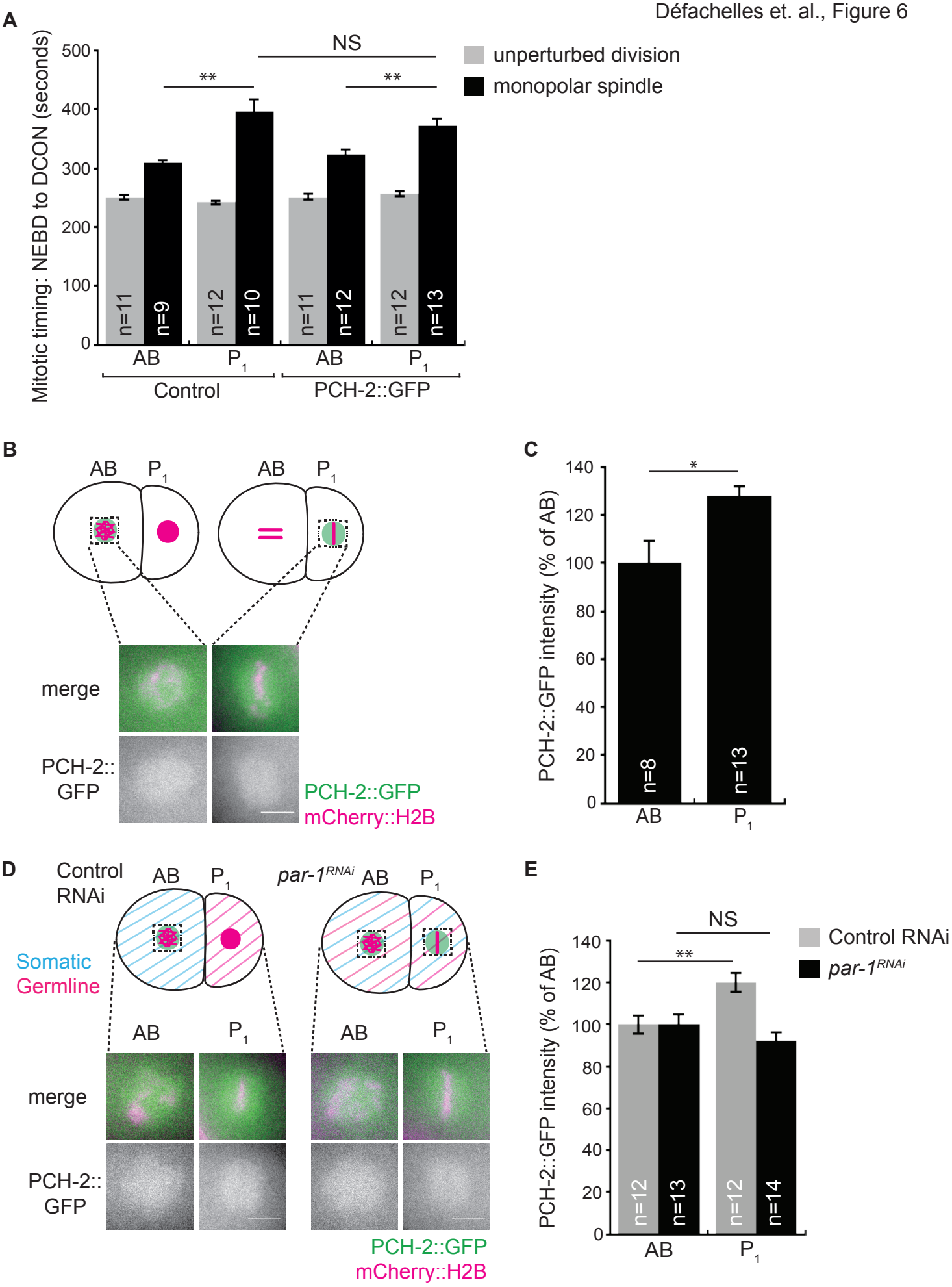

Défachelles et. al., Figure 7

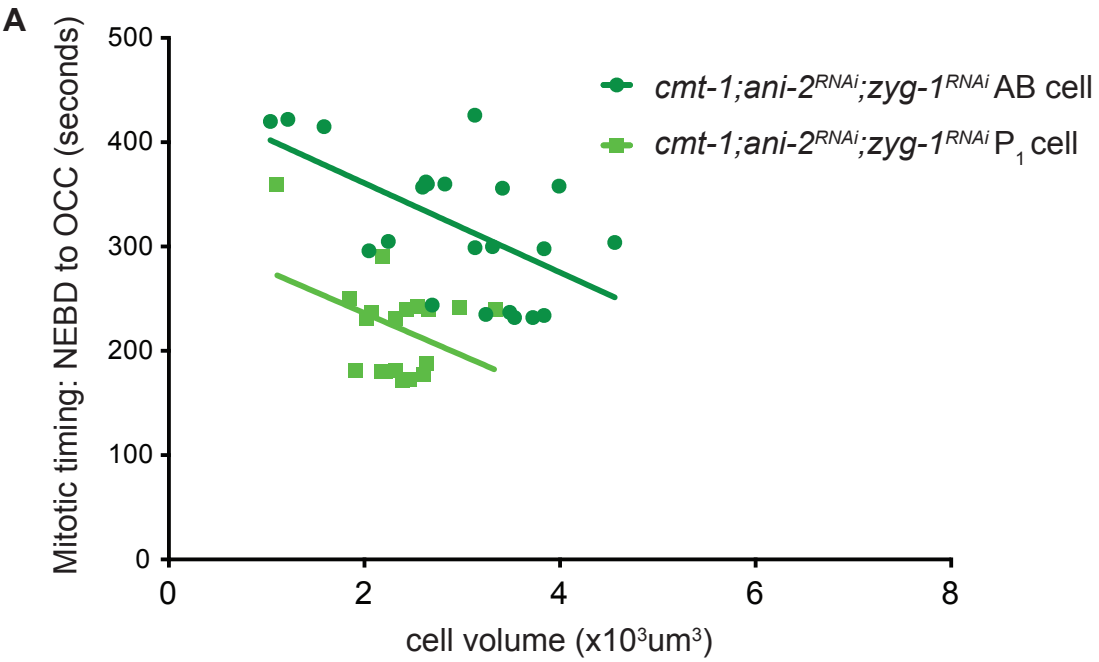

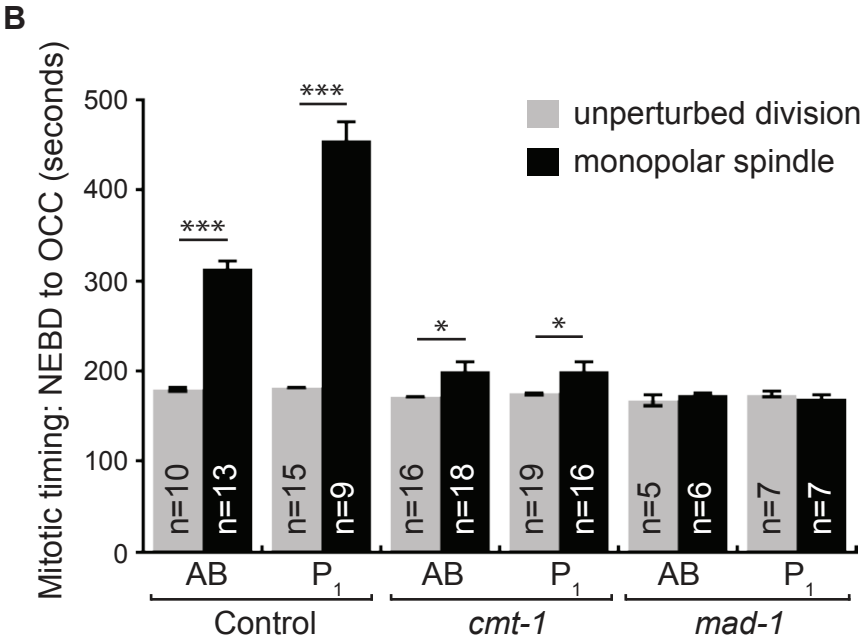

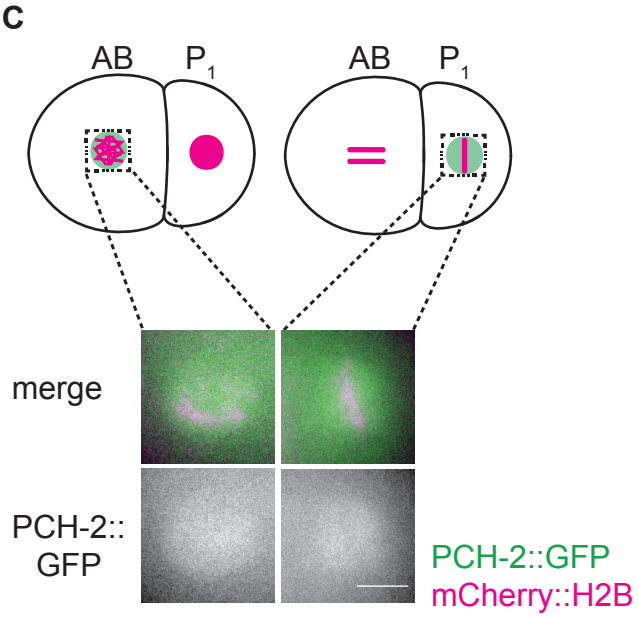

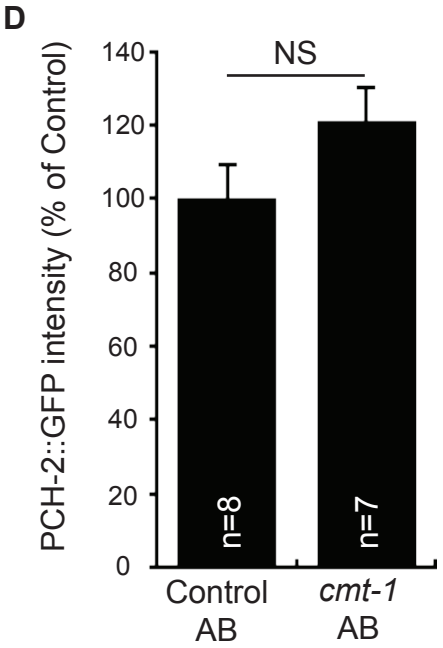

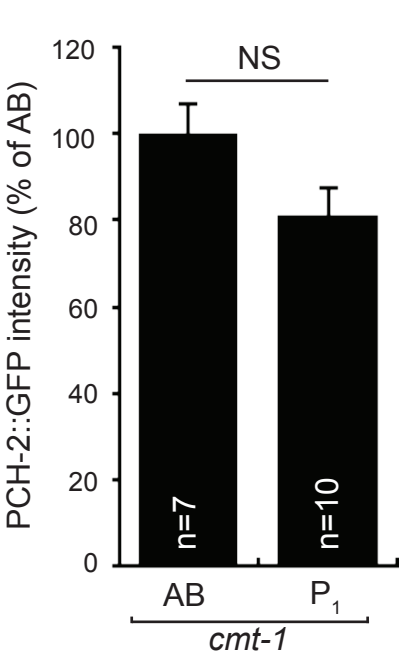

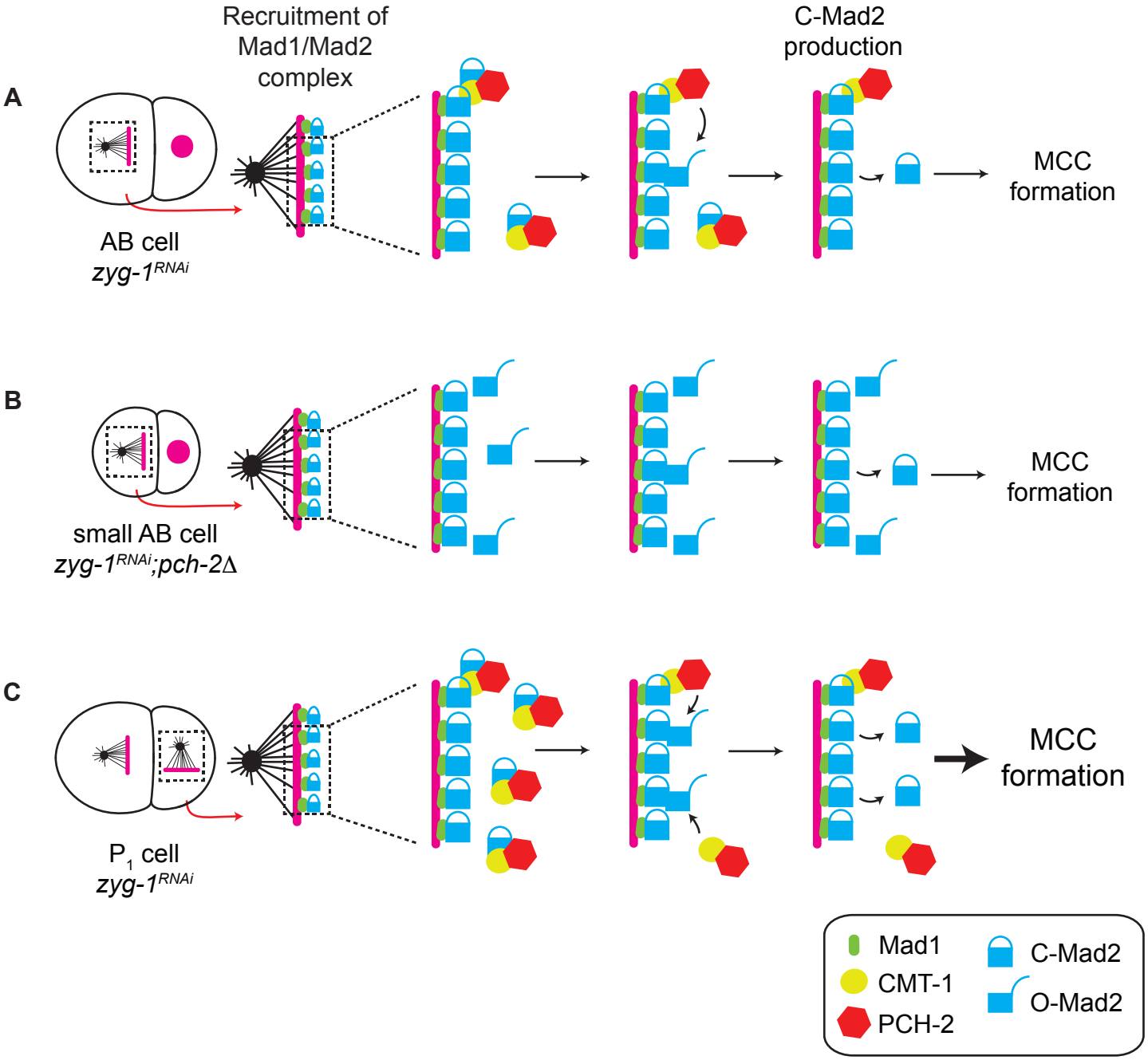
A
Recruitment of
Mad1/Mad2
complex
C-Mad2
production
AB cell
zyg-1RNAi
MCC
formation
B
small AB cell
zyg-1RNAi;pch-2Δ
MCC
formation
C
P1 cell
zyg-1RNAi
MCC
formation
Mad1
CMT-1
PCH-2
C-Mad2
O-Mad2

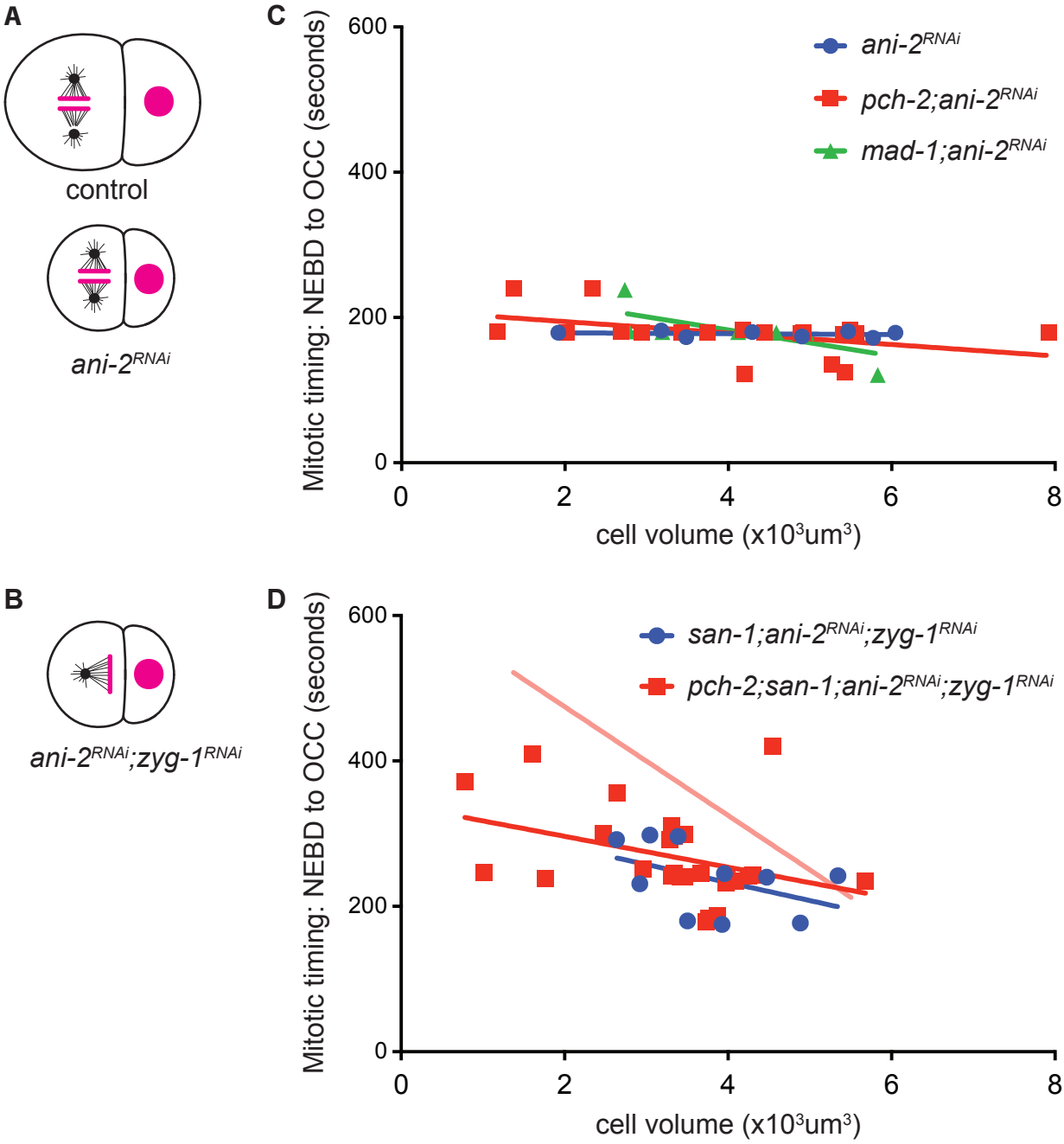
A
control
ani-2RNAi
B
ani-2RNAi;zyg-1RNAi
C
ani-2RNAi
pch-2;ani-2RNAi
mad-1;ani-2RNAi
Mitotic timing: NEBD to OCC (seconds)
cell volume (x10³um³)
D
san-1;ani-2RNAi;zyg-1RNAi
pch-2;san-1;ani-2RNAi;zyg-1RNAi
Mitotic timing: NEBD to OCC (seconds)
cell volume (x10³um³)

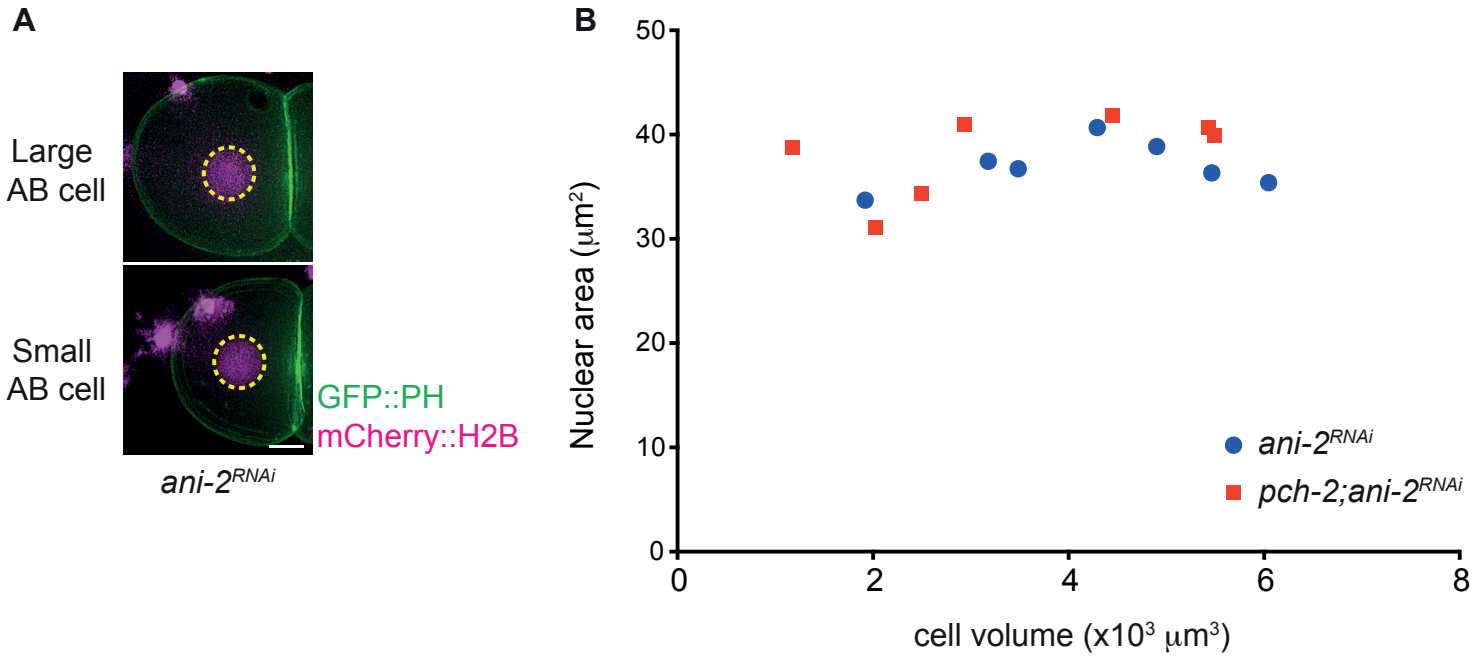
A
Large AB cell
Small AB cell
GFP::PH
mCherry::H2B
ani-2RNAi
B
Nuclear area (μm2)
cell volume (x103 μm3)
ani-2RNAi
pch-2;ani-2RNAi
0
10
20
30
40
50
0
2
4
6
8

Défachelles et. al., Figure S3

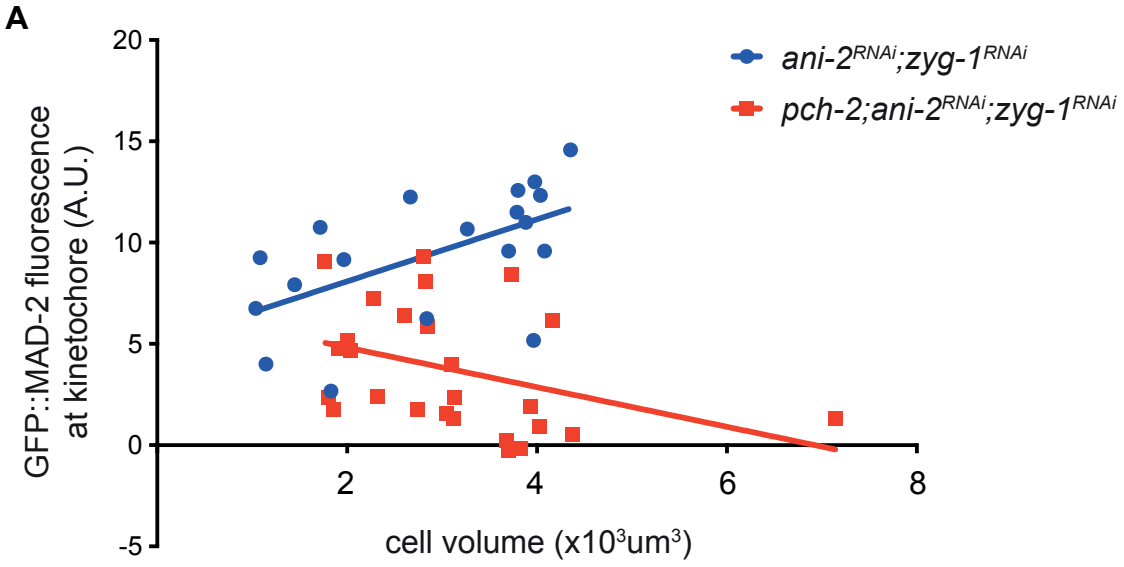

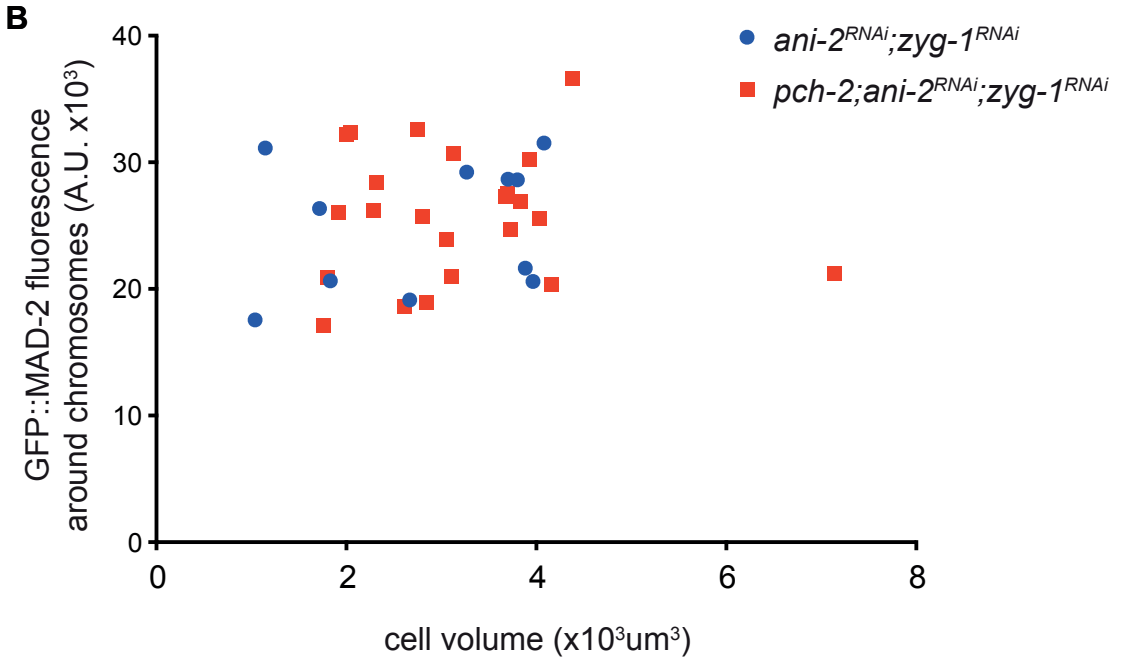

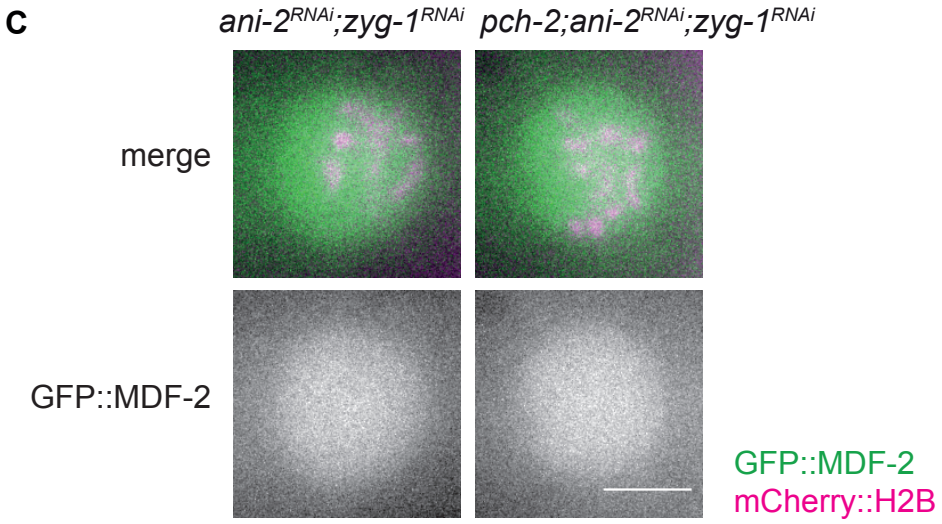

Défachelles et. al., Figure S4

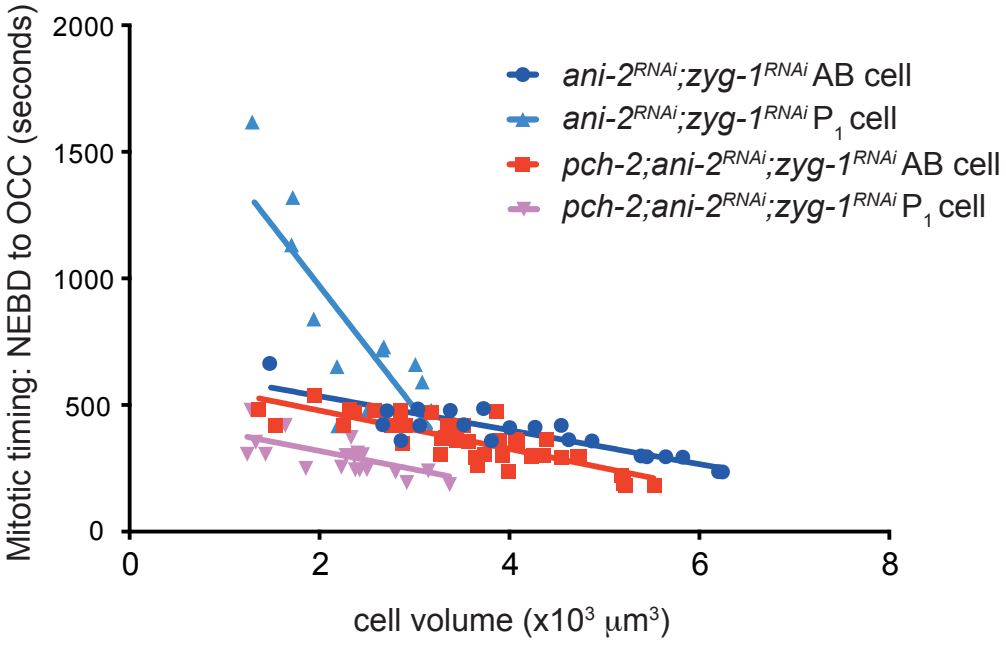

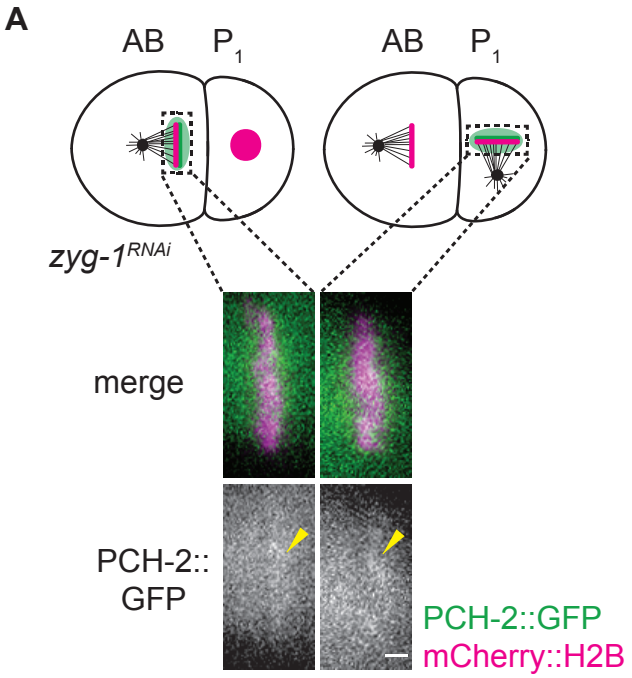
A
AB
P1
AB
P1
zyg-1RNAi
merge
PCH-2::
GFP
PCH-2::GFP
mCherry::H2B

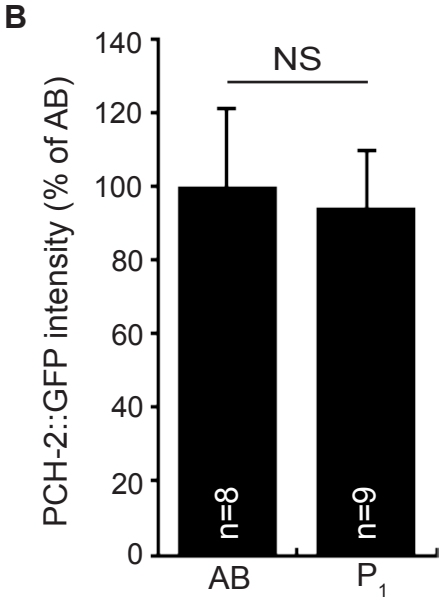
B
NS
PCH-2::GFP intensity (% of AB)
140
120
100
80
60
40
20
0
n=8
n=9
AB
P1

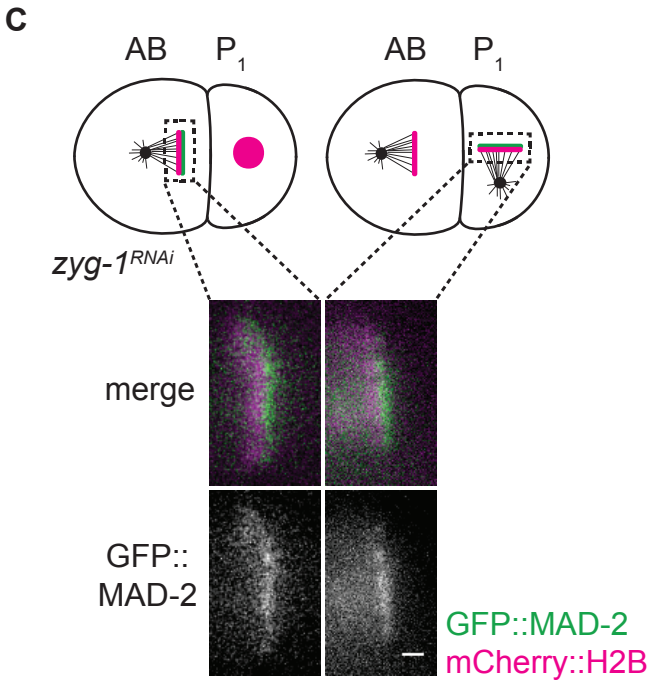
C
AB
P1
AB
P1
zyg-1RNAi
merge
GFP::
MAD-2
GFP::MAD-2
mCherry::H2B

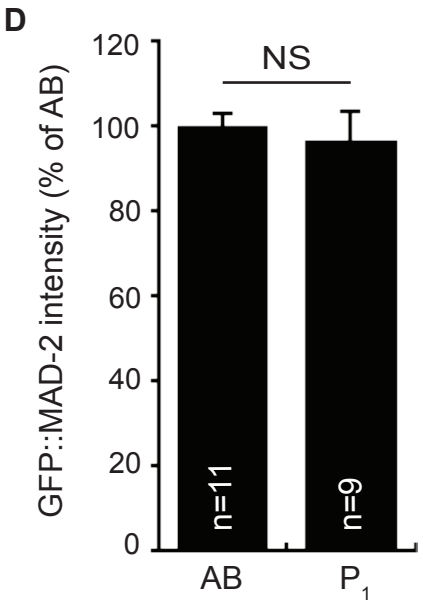
D
NS
GFP::MAD-2 intensity (% of AB)
120
100
80
60
40
20
0
n=11
n=9
AB
P1

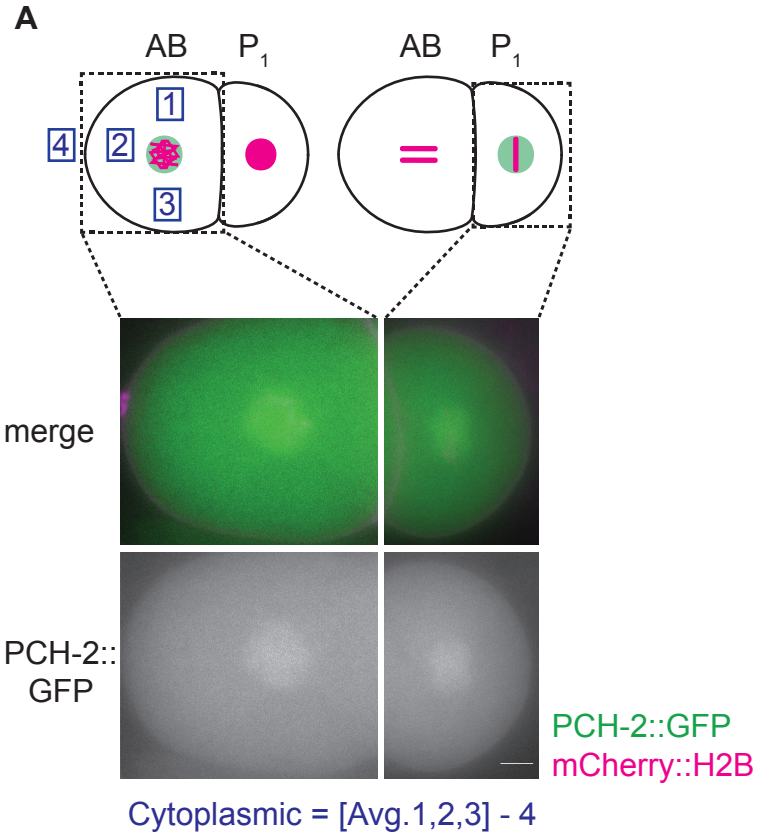
A
AB
P1
AB
P1
1
2
3
4
merge
PCH-2::
GFP
PCH-2::GFP
mCherry::H2B
Cytoplasmic = [Avg.1,2,3] - 4

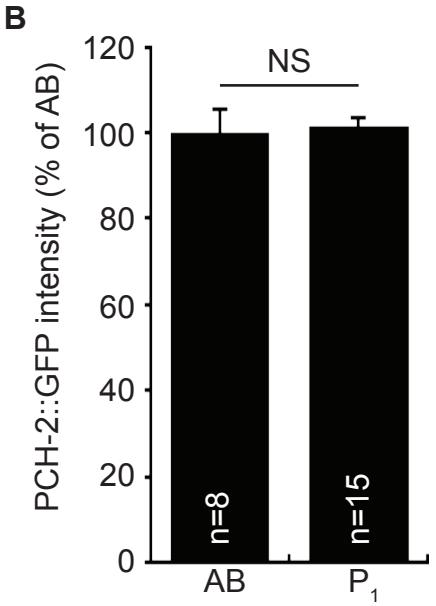
B
PCH-2::GFP intensity (% of AB)
120
100
80
60
40
20
0
NS
n=8
n=15
AB
P1

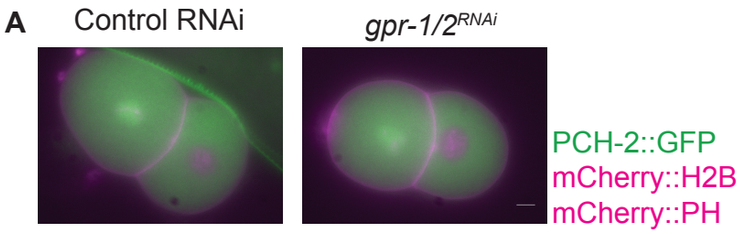
A
Control RNAi
gpr-1/2RNAi
PCH-2::GFP
mCherry::H2B
mCherry::PH

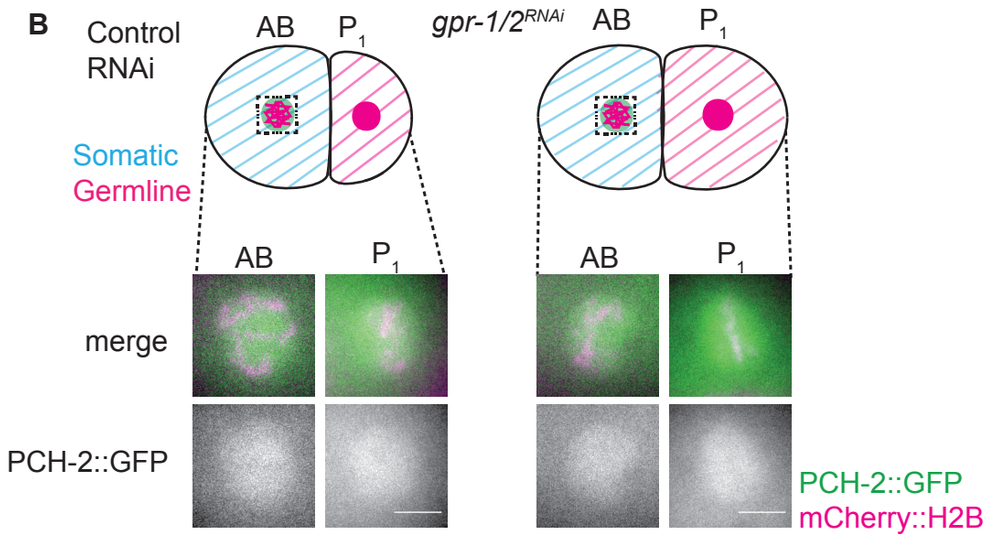
B
Control RNAi
AB
P1
gpr-1/2RNAi
AB
P1
Somatic
Germline
AB
P1
AB
P1
merge
PCH-2::GFP
PCH-2::GFP
mCherry::H2B

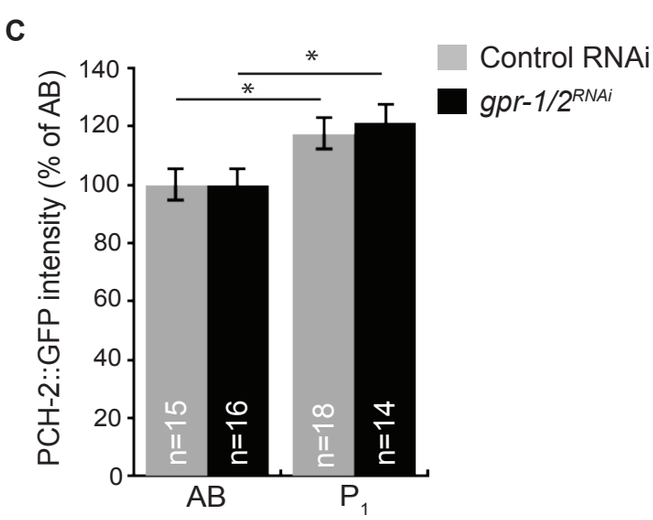
C
PCH-2::GFP intensity (% of AB)
140
120
100
80
60
40
20
0
*
*
Control RNAi
gpr-1/2RNAi
n=15
n=16
n=18
n=14
AB
P1

Table S1: Strains used in this study

Strain	Genotype
OD56	*unc-119(ed3) III; ltIs37 [pAA64; Ppie-1::mCherry::his-58; unc-119 (+)] IV*
OD95	*unc-119(ed3) III; ltIs37 [pAA64; Ppie-1::mCherry::his-58; unc-119 (+)] IV; ltIs38 [pAA1; Ppie-1::GFP::PH(PLC1delta1); unc-119(+)]*
BHL575	*pch-2(tm1458) II; unc-119(ed3) III; ltIs37 [pAA64; Ppie-1::mCherry::his-58; unc-119 (+)] IV; ltIs38 [pAA1;Ppie-1::GFP::PH(PLC1delta1); unc-119(+)]*
BHL596	*unc-119(ed3) III; ltIs37 [pAA64; Ppie-1::mCherry::his-58; unc-119 (+)] IV; ltIs38 [pAA1; Ppie-1::GFP::PH(PLC1delta1); unc-119(+)]; mdf-1(av19) V*
BHL600	*unc-119(ed3) III; ltIs37 [pAA64; Ppie-1::mCherry::his-58; unc-119 (+)] IV; ltIs52 [pOD379; Ppie-1::GFP::MDF-2; unc-119 (+)]*
BHL604	*pch-2(tm1458) II; unc-119(ed3) III; ltIs37 [pAA64; Ppie-1::mCherry::his-58; unc-119 (+)] IV; ltIs52 [pOD379; Ppie-1::GFP::MDF-2; unc-119 (+)]*
BHL608	*cmt-1(ok2879) I; unc-119(ed3) III; ltIs37 [pAA64; Ppie-1::mCherry::his-58; unc-119 (+)] IV; ltIs38 [pAA1;Ppie-1::GFP::PH(PLC1delta1); unc-119(+)]*
BHL664	*Ppch-2::pch-2::GFP-3XFLAG (blt4 [pCN94]) II; unc-119(ed3) III; ltIs37 [pAA64; Ppie-1::mCherry::his-58; unc-119 (+)] IV*
BHL666	*unc-119(ed3) III; ltIs37 [pAA64; Ppie-1::mCherry::his-58; unc-119 (+)];mdf-2(tm2190) IV/nT1[qIs51](IV;V) ltIs38 [pAA1; Ppie-1::GFP::PH(PLC1delta1); unc-119(+)]*
BHL883	*san-1/mdf-3 (ok1580) I; pch-2(tm1458) II; unc-119(ed3) III; ltIs37 [pAA64; Ppie-1::mCherry::his-58; unc-119 (+)] IV; ltIs38 [pAA1; Ppie-1::GFP::PH(PLC1delta1); unc-119(+)]*
BHL887	*cmt-1(ok2879) I; pch-2::GFP-3XFLAG (blt4 [pCN94]) II; unc-119(ed3) III; ltIs44[pAA173; pPie-1::mCherry::PH(PLC1delta1); unc-119(+)]; ltIs37 [pAA64; Ppie-1::mCherry::his-58; unc-119 (+)] IV*
BHL888	*unc-119(ed3) III; ltIs44 [pAA173; pPie-1::mCherry::PH(PLC1delta1); unc-119(+)]; ltIs52 [pOD379; Ppie-1::GFP::mdf-2; unc-119 (+)]; ltIs37 [pAA64; Ppie-1::mCherry::his-58; unc-119 (+)] IV*
BHL889	*pch-2(tm1458) II; unc-119(ed3) III; ltIs44 [pAA173; pPie-1::mCherry::PH(PLC1delta1); unc-119(+)]; ltIs52 [pOD379; Ppie-1::GFP::mdf-2; unc-119 (+)]; ltIs37 [pAA64; Ppie-1::mCherry::his-58; unc-119 (+)] IV*
BHL891	*unc-119(ed3) III; ltIs37 [pAA64; Ppie-1::mCherry::his-58; unc-119 (+)] IV; ltIs24[pAZ132; pPie-1::GFP::tba-2; unc-119(+)]*
BHL892	*pch-2 (tm1458) II; unc-119(ed3) III; ltIs37 [pAA64; Ppie-1::mCherry::his-58; unc-119 (+)] IV; ltIs24 [pAZ132; pPie-1::GFP::tba-2; unc-119(+)]*
BHL893	*san-1/mdf-3 (ok1580) I; unc-119(ed3) III; ltIs37 [pAA64; Ppie-1::mCherry::his-58; unc-119 (+)] IV; ltIs38 [pAA1; Ppie-1::GFP::PH(PLC1delta1); unc-119(+)]*
BHL904	*Ppch-2::pch-2::GFP-3XFLAG (blt4 [pCN94]) II; unc-119(ed3) III; ltIs44[pAA173; pPie-1::mCherry::PH(PLC1delta1); unc-119(+)]; ltIs37 [pAA64; Ppie-1::mCherry::his-58; unc-119 (+)] IV*
BHL950	*pch-2(tm1458) II; unc-119(ed3) III; ltIs37 [pAA64; Ppie-1::mCherry::his-58; unc-119 (+)]; mdf-2(tm2190) IV/nT1[qIs51](IV;V); ltIs38 [pAA1; Ppie-1::GFP::PH(PLC1delta1); unc-119(+)]*

BHL958	*unc-119(ed3) III; ltIs37 [pAA64; Ppie-1::mCherry::his-58; unc-119 (+)] IV/nT1[qIs51](IV;V); ltIs38 [pAA1; Ppie-1::GFP::PH(PLC1delta1); unc-119(+)]*
BHL964	*zyg-1(or297) unc-4(e120) II unc-119(ed3) III; ltIs37 [pAA64; Ppie-1::mCherry::his-58; unc-119 (+)] IV; ltIs24[pAZ132; pPie-1::GFP::tba-2; unc-119(+)]*
BHL965	*zyg-1(or297) pch-2(tm1458) unc-4(e120) II; unc-119(ed3) III; ltIs37 [pAA64; Ppie-1::mCherry::his-58; unc-119 (+)] IV; ltIs24[pAZ132; pPie-1::GFP::tba-2; unc-119(+)]*
GAL5	*san-1/mdf-3 (mat5) I; unc-119(ed3) III; ruIs57[Ppie-1::GFP::tubulin + unc-119(+)]; ltIs37[pie-1p::mCherry::his-58 (pAA64) + unc-119(+)] IV*